

Geochemical constraints on the mobilization of Ni and critical metals in laterite deposits, Sulawesi, Indonesia: A mass - balance approach

Ito, Akane

Department of Applied Chemistry for Environment School of Science and Technology, Kwansei Gakuin University

Otake, Tsubasa

Division of Sustainable Resource Engineering, Faculty of Engineering, Hokkaido University

Maulana, Adi

Department of Geological Engineering Hasanuddin University

Sanematsu, Kenzo

Institute for Geo - Resources and Environment, National Institute of Advanced Industrial Science and Technology

他

<https://hdl.handle.net/2324/7177960>

出版情報 : Resource Geology. 71 (3), pp.255-282, 2021-05-12. Wiley

バージョン :

権利関係 : © 2021 Society of Resource Geology



Geochemical constraints on the mobilization of Ni and critical metals in laterite deposits, Sulawesi, Indonesia: A mass-balance approach

Akane Ito¹  | Tsubasa Otake²  | Adi Maulana³  | Kenzo Sanematsu⁴  |
Sufriadin⁵  | Tsutomu Sato² 

¹Department of Applied Chemistry for Environment, School of Science and Technology, Kwansei Gakuin University, Sanda, Japan

²Division of Sustainable Resource Engineering, Faculty of Engineering, Hokkaido University, Sapporo, Japan

³Department of Geological Engineering, Hasanuddin University, Makassar, Indonesia

⁴Institute for Geo-Resources and Environment, National Institute of Advanced Industrial Science and Technology, Tsukuba, Japan

⁵Department of Mining Engineering, Hasanuddin University, Makassar, Indonesia

Correspondence

Akane Ito, Department of Applied Chemistry for Environment, School of Science and Technology, Kwansei Gakuin University, 2-1 Gakuen, Sanda 669-1337, Japan.

Email: aito@kwansei.ac.jp

Funding information

Grant-in-Aid for Japan Society for the Promotion of Science Fellows, Grant/Award Number: 18J11243; Japan Society for the Promotion of Science, Grant/Award Number: KAKENHI (17H03502); Japan Society for the Promotion of Science, Grant/Award Number: KAKENHI (19K24388)

Abstract

Indonesia is one of the largest Ni ore producers in the world and is also expected to be an important potential source of some critical metals (e.g., Co, Sc, rare-earth elements, and platinum-group elements). However, few studies have examined Ni laterite deposits in this country. In this study, we investigate Ni enrichment and the potential accumulation of critical metals in four laterite profiles with varying degrees of serpentinization and weathering intensity in the Soroako and Pomalaa mining areas of Sulawesi, Indonesia. We integrate geochemical evaluation with a mass-balance approach and mineralogical analysis to better constrain the geochemical factors influencing the mobilization of Ni during lateritization. Nickel contents in the saprolite horizon of the profiles that are strongly weathered and developed over serpentinized peridotite are higher than those that are weakly weathered and developed over unserpentinized harzburgite. The bulk Ni contents of saprolite horizons are related to Ni contents of Ni-bearing Mg-phyllsilicates, which suggests that Ni remobilization is the main control on Ni enrichment in the profiles. Mass-balance calculations reveal that the amounts of gained Fe and Ni in the profiles are positively correlated. This relationship indicates that the redistribution of Ni is likely controlled by the aging of Ni-bearing goethite (dissolution/recrystallization) involving ligand-promoted dissolution by organic matter and/or reductive dissolution by microbial activity near the surface. Critical metals show enrichment in specific horizons. Enrichments in Co and rare-earth elements are strongly influenced by the formation of Mn-oxyhydroxides in the oxide zone of the profiles. In contrast, Sc, Pt, and Pd show residual enrichment patterns, with grades influenced mainly by their initial contents in bedrock. The profiles show a positive correlation between Sc and Fe, as reported for other Ni laterite deposits. Among the critical metals, Sc, Pt, and Pd contents in the studied profiles are comparable with values reported from other Ni laterite deposits worldwide.

KEYWORDS

critical metal, Indonesia, mass balance calculation, nickel laterite, supergene enrichment, ultramafic rock

1 | INTRODUCTION

Nickel laterite deposits, which form by intensive chemical weathering of mafic to ultramafic rocks under tropical environments, account for over 60% of both the world's land-based Ni resource and annual global Ni production (McRae, 2020). During chemical weathering, meteoric waters interact with ultramafic rocks, leading to the dissolution of primary silicates and leaching of soluble elements (e.g., Si and Mg) as well as the accumulation of less soluble elements such as Fe as (oxy)hydroxides (e.g., goethite) in the oxide zone (also known as “limonite” or “laterite”). Nickel that is leached by the dissolution of silicates and involved in the evolution of Ni-bearing goethite (dissolution/recrystallization) is transported downward by the percolation of soil water and subsequently captured by secondary (Ni)–Mg phyllosilicates (e.g., serpentine, smectite, and talc-like minerals) in the saprolite horizon. This supergene process, the so-called *per descensum* process, has been invoked to explain the formation of economic-grade ores (e.g., Trescases, 1975; Cluzel and Vigier, 2008), especially high-grade saprolite ores. However, the distribution of Ni is strongly influenced by many interacting factors, including lithology, tectonic setting, drainage, climate, and the presence of organic matter (e.g., Golightly, 1981; Gleeson *et al.*, 2003; Freyssinet *et al.*, 2005; Golightly, 2010; Thorne *et al.*, 2012; Butt and Cluzel, 2013; Maurizot *et al.*, 2019). These multiple interacting factors cause spatial heterogeneity in Ni grade, even in a single deposit.

Recently, Ni laterite deposits have also been considered as potential targets for the exploration of some critical metals, such as Co, Sc, rare earth elements (REEs), and platinum group elements (PGEs), in response to the rapid growth in demand for these elements (Chakhmouradian and Wall, 2012) and improved extraction via the development of high-pressure acid leaching for the recovery of important metals as by-products from low-grade oxide ores or tailings (Wang *et al.*, 2011). Several studies have investigated the potential occurrence of critical metals in Ni laterite deposits in Cuba and the Dominican Republic (Aiglsperger *et al.*, 2015, 2016), Australia (Chasse *et al.*, 2017; Putzolu *et al.*, 2018; Chasse *et al.*, 2019; Putzolu *et al.*, 2019), New Caledonia (Audet, 2008; Traore *et al.*, 2008a, 2008b; Teitler *et al.*, 2019; Ulrich *et al.*, 2019), and central Africa (Dzemua *et al.*, 2013).

Many large-scale Ni laterite deposits have been discovered on Sulawesi Island (Indonesia) and are well developed on peridotites of obducted ophiolite suites subjected to humid and hot climatic conditions. These deposits have allowed Indonesia to become the world's major producer of Ni (McRae, 2020). The Soroako and Pomalaa mining areas, which are located in the central and southeastern parts of Sulawesi Island, respectively, are the two largest Ni laterite mining sites in Sulawesi Island and produce mainly Ni-rich saprolite ore. Despite their major economic importance, few investigations have been made into the geochemical characteristics of Indonesian Ni laterites (Golightly and Arancibia, 1979; Golightly, 1981; Sufriadin *et al.*, 2011; Ilyas and Koike, 2012; Fu *et al.*, 2014; Ilyas *et al.*, 2016; Farrokhpay *et al.*, 2019). There is also a lack of data on the distribution of critical metals (e.g., Maulana *et al.*, 2016).

In this study, we investigate the geochemistry and mineralogy of four laterite profiles that show variations in parent rock-type and degree of weathering in the Soroako and Pomalaa mining areas, and integrate the resulting information with mass-balance calculations to constrain the behavior of Ni in the laterite profiles, particularly the geochemical factors controlling the remobilization of Ni during laterization. We also apply these calculations to Ni laterites located in other tropical regions and compare the results with those of the studied Indonesian profiles. Finally, we present an overview of the distribution of critical metals (Co, Sc, REEs, Pt, and Pd) through the weathering profiles and infer the geochemical processes involved in their enrichment.

2 | GEOLOGICAL SETTING

Sulawesi Island, in central Indonesia, is located at the convergent margin of the Eurasian, Pacific–Philippines, and Indian–Australian plates. It contains four lithotectonic belts from west to east: the West Sulawesi Plutono-Volcanic Arc Belt, the Central Sulawesi Metamorphic Belt, the East Sulawesi Ophiolite (ESO) Belt, and continental fragments of the Banggai–Sula islands and Tukang Besi–Buton platforms (Mubroto *et al.*, 1994; Hall and Wilson, 2000; Kadarusman *et al.*, 2004; Maulana *et al.*, 2013; Figure 1a). The ESO is tectonically dismembered and widely distributed from Gorontalo Bay through the East Arm and central Sulawesi toward the

Southeast Arm and the islands of Buton and Kabaena (Mubroto *et al.*, 1994; Hall and Wilson, 2000; MacPherson and Hall, 2002; Kadarusman *et al.*, 2004). Ni laterites are located mostly in a complex of Cretaceous ultramafic rocks in eastern Sulawesi, which was exposed during Miocene convergence at ~10 Ma (Golightly, 1979; Suratman, 2000; Kadarusman *et al.*, 2004).

The Soroako mining area in southern Sulawesi province and the Pomalaa mining area in southeastern Sulawesi province are the two largest Ni laterite mining sites in Indonesia and are located in the ESO (Figure 1a). In

the Soroako mining area, harzburgite and dunite, which are cut by pyroxenite and gabbroic dikes, are dominant over lherzolite (Kadarusman *et al.*, 2004). These peridotites have been variably metamorphosed, ranging from fresh peridotite to serpentinite. Two additional lithological units (Quaternary alluvial and lacustrine rocks, and Cretaceous sedimentary rocks) occur around the ultramafic rocks.

In this study, we investigated three laterite profiles in the Soroako mining area: Watulabu Hill, Konde Hill, and a hill in the Petea Block (hereafter “Petea Hill”).

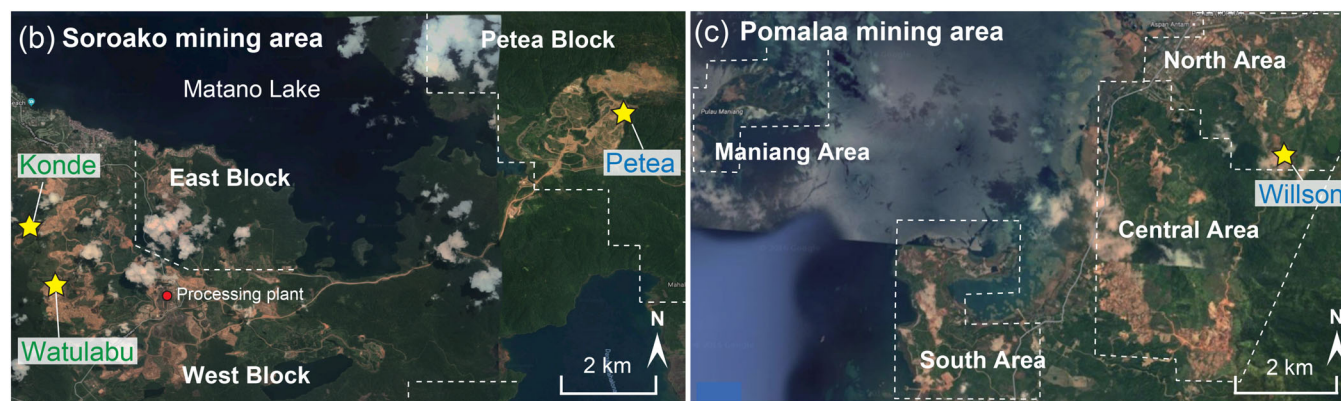
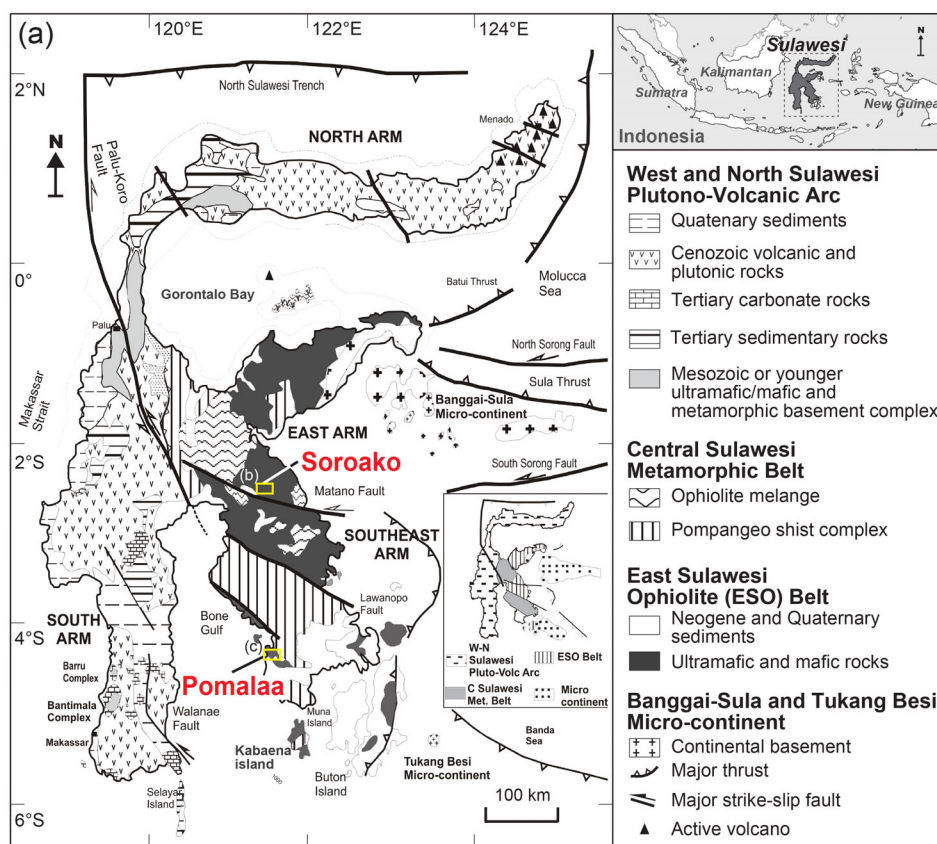


FIGURE 1 (a) Geological map of Sulawesi Island in Indonesia, showing the locations of the Soroako and Pomalaa mining areas (after Kadarusman *et al.*, 2004 and Maulana *et al.*, 2013). (b and c) Satellite maps showing the locations of (b) Watulabu, Konde, and Petea hills in the Soroako mining area and (c) Willson Hill in the Pomalaa mining area

The Soroako mining area is divided into several blocks based on lithology. Watulabu Hill and Konde Hill are located in the West Block, in the area to the southwest of Lake Matano, which is characterized geologically by underlying unserpentinized harzburgite or minor dunite and topographically by rounded hills, terraces, and ridges (Figure 1b). In contrast, the Petea Block, in the area to the southeast of Lake Matano, is developed on serpentinized harzburgite and is characterized topographically by steep plateaus and terrace-like morphology in the northern part of the block and by graben-like features or lowland depressions in the southern part (Figure 1b).

In contrast, ultramafic rocks in the Pomalaa mining area occur as small irregular-shaped, isolated bodies (van Leeuwen and Pieters, 2011; Figure 1a). In this area, ultramafic rocks are mostly serpentinized (Simandjuntak *et al.*, 1991). One profile, that of Willson Hill, located in the southeastern end of North Area in the northern part of the mining area, was investigated (Figure 1c). The bedrock lithology of Willson Hill is serpentinized harzburgite, and the terrain is relatively subdued with gentle slopes.

Figure 2a presents schematic columnar views of the studied profiles, which show that the thickness of laterite profiles varies from 8 to 32 m. Petea Hill has the best-

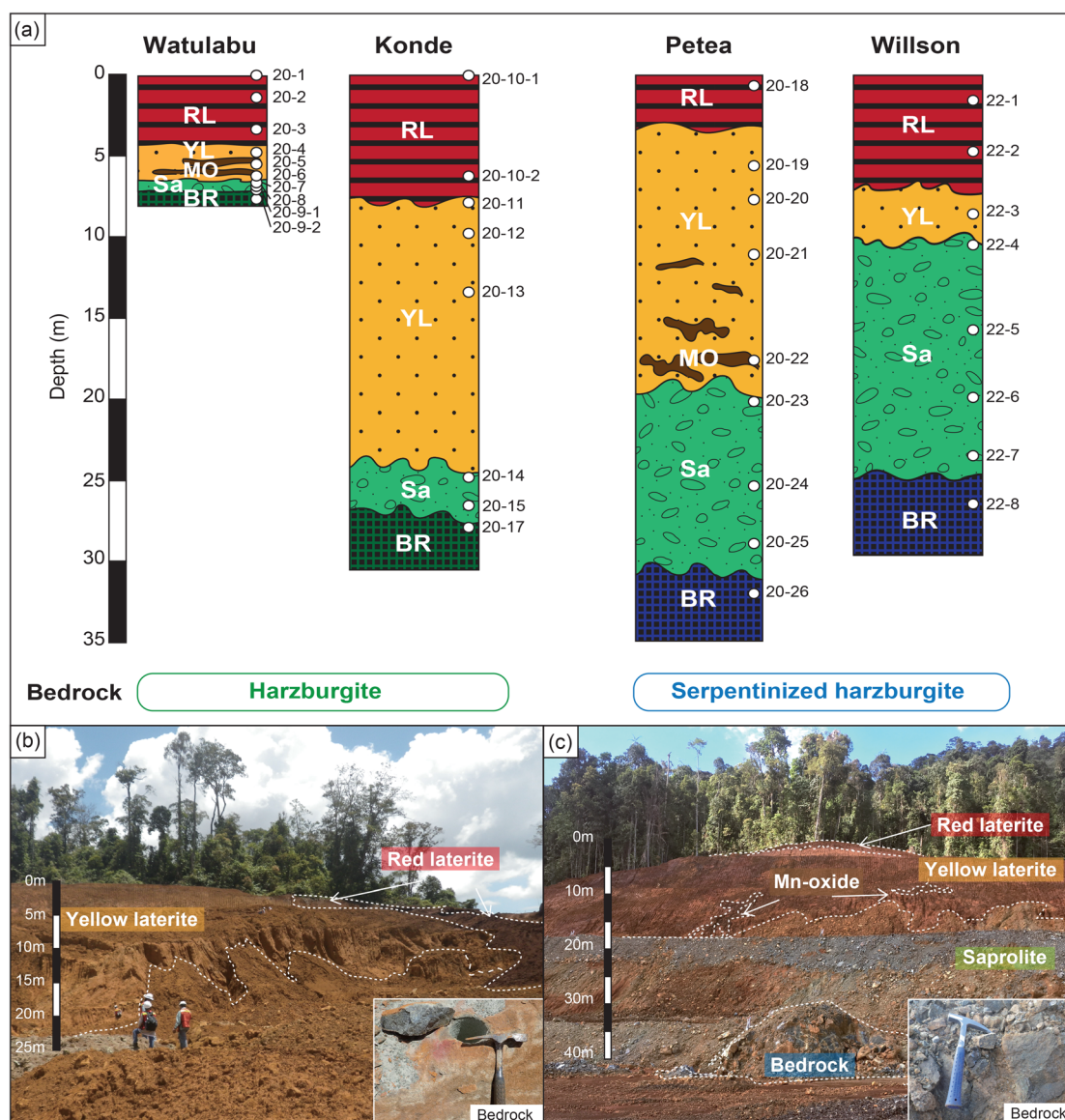


FIGURE 2 (a) Schematic columnar view of each hill profile, showing locations of samples and lithological horizons (RL, red laterite; YL, yellow laterite; MO, Mn-oxide; Sa, sapolite; BR, bedrock). (b and c) Representative cross-sections of (b) the oxide-zone-dominated profile overlying fresh peridotite of Konde Hill and (c) the sapolite-dominated profile overlying serpentinized peridotite of Petea Hill

developed profile with a thickness of 32 m, slightly thicker than those at Konde Hill (27 m) and Willson Hill (26 m) and much thicker than that at Watulabu Hill (8 m). Watulabu and Konde hills, which are developed on unserpentinized harzburgite, have thicker oxide zones relative to saprolite zones, whereas Petea and Willson Hills, which overlie serpentinized harzburgite, have thicker saprolite zones relative to oxide zones (Figure 2a). Representative cross-sections showing a thick laterite horizon at Konde Hill and a thick saprolite horizon at Petea Hill are presented in Figure 2b,c, respectively. The laterite profiles observed at the studied sites are divided from bottom to top into bedrock, saprolite, yellow laterite, and red laterite. A discontinuous and thin Mn-oxyhydroxide-rich horizon (hereafter “Mn-oxide horizon”) is locally present at the bottom of oxide zones (Figure 2a). These lithological classifications are based mainly on variations in color, texture, and mineralogy. In this study, the term “oxide zone” is used for the overall laterite horizon, whereas “red laterite” and “yellow laterite” are used to distinguish the sub-horizons in the oxide zone.

3 | SAMPLING AND ANALYTICAL METHODS

Samples of bedrock and laterite were collected from vertical profiles, with at least one sample being obtained from each horizon, except for Mn-oxide samples, which were collected only from Watulabu and Petea hills (Table 1, Figure 2a).

Laterite samples were dried at 40°C, homogenized, and quartered. Bedrock samples and dried laterite samples were then pulverized to ~75 µm by using a multi-bead shocker (PV1001[s], Yasui Kikai) with an agate rod and polycarbonate tube for subsequent analysis. For porewater pH measurements, 10 g of pulverized laterite sample and 25 g of deionized water were placed in 50 ml centrifuge tubes and shaken for 2 hr at 150 rpm at room temperature. After centrifuging for 30 min at 2,000 rpm, pH values of the supernatant solution were measured at room temperature. Loss on ignition (LOI) was determined for all samples by calculation of the change in mass before and after combustion of samples at 1,000°C for 12 hr in a muffle furnace.

Contents of major elements, some minor elements (Mn, Co, and Ni), and Sc were determined on fused glass beads by X-ray fluorescence (XRF; MagiX PRO, Spectris). The glass beads were obtained by fusing the mixtures of 0.4 g of post-combustion sample and 4 g of lithium tetraborate at 1200°C in a Pt crucible using a high-frequency fusion instrument (TK-4100, Amena

Tech). A small portion (30 mg) of each pulverized sample was dissolved by heating in a high-pressure stainless bomb, consisting of a 4 ml PTFE inner vessel and an outer stainless pressure jacket, with a mixture of 0.5 ml of concentrated HF (ultrapure grade; Kanto Chemical) and 0.5 ml of concentrated HNO₃ (ultrapure grade; Kanto Chemical) at 180°C for 72 hr. The residues were dried and redissolved in 1 ml of 6 M HCl (ultrapure grade; Kanto Chemical), then heated at 180°C for 24 hr. After drying the solutions, the dried samples were dissolved in 1 ml of 1% HNO₃, following which the content of REEs (La to Lu) was acquired by using inductively coupled plasma-mass spectroscopy (ICP-MS; iCap Qc, Thermo Scientific). Pd and Pt contents were obtained at Actlabs (Ontario, Canada) by ICP-MS (detection limits of 0.1 ppb for Pd and Pt) after nickel sulfide fire assay collection, following the method described by Hoffman and Dunn (2002).

X-ray powder diffraction (XRPD; Multi Flex, Rigaku) analysis was performed with Cu-Kα radiation at 40 kV and 30 mA with graphite-monochromator to determine mineralogical compositions. Randomly oriented powder samples were scanned from 5 to 70° (2θ) with a scanning rate of 2.0°/min. Mineral identification was obtained by using Match! software version 3.0 (Crystal Impact). To confirm the presence of expandable clay silicates (e.g., smectite) in the saprolite samples, the <2 µm fraction was separated from the coarse sample by ultrasonic dispersion and centrifugation. Oriented aggregate samples were prepared by mounting the suspended solution of the <2 µm fraction on glass slides and drying at room temperature. These oriented samples were then treated under ethylene glycol saturated conditions at 60°C overnight. The XRPD patterns of samples on oriented mounts were obtained by XRPD (RINT 2000, Rigaku) analysis with Cu-Kα radiation at 30 kV and 20 mA. The samples were scanned from 2 to 40° (2θ) at a scanning rate of 0.02°/s.

Mineral phases and textural features were examined on polished thin sections under a scanning electron microscope coupled to an energy dispersive spectrometer (SEM-EDS; JSM-6510LA, JEOL). Field emission-electron probe microanalyses (FE-EPMA; JXA-8530F, JEOL) were performed on representative polished thin sections with a wavelength dispersive X-ray spectrometer to determine the chemical composition of Ni-bearing minerals in saprolite and bedrock samples. Serpentine and smectite were identified based on the measured (Mg + Fe + Ni)/Si ratios compared with the stoichiometric ratios (i.e., 1.5 for serpentine and 0.6–0.8 for smectite). The structural formulae for serpentine and smectite were calculated for 7 and 11 oxygens, respectively.

To determine the degree of chemical weathering of ultramafic rocks and laterite samples, a weathering

TABLE 1 Contents of relevant major and minor elements (wt%) and trace elements (ppm or ppb), and values of UMIA, pH, and $\tau_{Ti,j}$ for bedrock and laterite samples from laterite profiles in the Soroako (Watulabu Hill, Konde Hill, and Petea Hill) and Pomalaa (Willson Hill) mining areas

Mining area		Soroako																
Hill	Watulabu																	
Sample name	20-1	20-2	20-3	20-4	20-5	20-6	20-7	20-8	20-9-1	20-9-2	20-10-1	20-10-2	20-11	20-12	20-13	20-14	20-15	20-17
Sample type	RL	RL	RL	YL	MO	MO	Sa	Sa	Sa	BR	RL	RL	YL	YL	YL	Sa	Sa	BR
Depth (m)	0	1.3	3.3	4.6	5.9	6.3	6.6	6.7	7.0	7.5	0	6	7	9.5	13	24	26	27
Wt%																		
SiO ₂	2.19	7.42	3.07	15.4	4.32	24.3	29.5	38.1	39.4	43.8	1.60	1.04	1.52	1.55	2.86	52.2	70.5	43.2
Al ₂ O ₃	3.83	2.86	2.39	3.99	2.12	1.10	1.55	1.43	0.70	0.51	7.27	7.12	6.32	7.68	6.36	1.51	0.70	0.77
Fe ₂ O ₃	76.0	66.3	71.8	55.9	44.3	35.6	39.5	18.0	11.1	8.67	73.4	72.1	70.5	68.3	68.0	13.8	10.2	8.77
MnO	0.86	0.78	0.20	0.72	28.7	22.9	0.30	1.41	0.13	0.13	0.37	0.22	0.15	1.51	0.11	0.21	0.15	0.13
MgO	0.76	2.53	1.61	7.46	0.49	0.51	12.4	30.7	31.8	44.4	0.82	0.88	0.94	1.04	1.19	22.8	6.16	43.6
CaO	0.010	<0.003	0.003	0.303	0.010	0.013	0.013	0.600	0.137	0.589	0.005	0.009	0.004	0.008	0.003	0.986	0.190	0.891
Na ₂ O	0.19	0.18	0.18	0.16	0.19	0.19	0.13	0.06	0.04	0.01	0.18	0.18	0.17	0.17	0.18	0.12	0.18	0.01
K ₂ O	0.003	<0.004	<0.004	0.004	0.021	0.010	0.010	0.007	0.006	0.008	0.004	0.005	0.005	<0.004	0.003	0.009	0.014	0.009
TiO ₂	0.04	0.03	0.03	0.05	0.02	0.02	0.02	0.04	0.01	0.01	0.14	0.14	0.07	0.08	0.06	0.02	0.01	0.03
P ₂ O ₅	0.010	0.008	0.007	0.008	0.008	0.007	0.008	0.006	0.007	0.007	0.031	0.032	0.011	0.010	0.011	0.007	0.007	0.008
Cr ₂ O ₃	2.75	3.44	4.74	3.06	1.62	1.68	2.16	0.78	0.68	0.40	3.45	4.24	3.08	2.67	2.67	1.02	0.52	0.45
CoO	0.071	0.077	0.085	0.085	1.197	0.616	0.059	0.042	0.143	0.015	0.036	0.017	0.048	0.199	0.027	0.023	0.018	0.015
NiO	1.70	3.10	2.03	2.60	1.44	1.00	2.78	1.80	2.75	0.30	1.67	1.22	2.38	2.31	2.73	0.76	0.47	0.29
LOI	12.9	13.2	12.2	11.3	14.0	10.7	10.6	5.7	12.4	0.7	12.7	12.9	14.9	15.3	15.1	3.8	8.7	0.8
ppm																		
Sc	36	49	33	47	42	24	11	22	10	3	61	56	60	72	56	21	9	11
V	190	229	185	210	141	92	108	79	53	41	284	289	254	293	262	95	44	40
Cr	18826	23554	32452	20923	11092	11514	14800	5354	4665	2761	23616	28989	21081	18292	18260	7003	3574	3069
Co	556	606	668	669	9417	4845	467	331	1128	117	283	137	376	1566	214	182	142	117
Ni	13371	24388	15941	20429	11331	7836	21856	14111	21634	2358	13160	9570	18674	18173	21418	5984	3682	2280
Cu	312	196	191	112	202	134	60	18	<1.6	95	313	246	266	255	231	139	19	146
Zn	573	722	703	597	984	327	368	177	406	51	462	386	416	461	446	68	51	62
ppb																		
La	4740	1848	7566	434	47937	41697	727	535	8129	9	628	385	350	455	312	17	44	4
Ce	19983	7693	2975	236	658	426	833	46	24	19	1909	1254	616	8760	4114	21	40	12
Pr	2297	484	409	101	1391	11903	220	16	30	2	139	93	121	153	178	5	7	2
Nd	9713	1808	1878	438	4378	46387	942	40	39	3	504	360	517	740	902	16	23	3
Sm	2915	350	712	74	404	4097	216	5	4	1	110	88	170	233	297	3	4	1
Eu	664	73	164	21	99	948	46	4	1	0	23	18	39	49	63	0.5	1	1
Gd	2539	307	568	121	912	8721	223	13	12	4	99	79	131	205	252	6	8	7

TABLE 1 (Continued)

Mining area		Soroako																Konde															
Hill		Watulabu																															
Tb		513	48	124	23	90	981	39	3	3	1	18	15	25	36	47	2	2	2	2	3												
Dy		3403	305	885	183	692	7126	259	32	25	11	118	100	173	236	294	21	15	15	24													
Ho		650	66	192	51	261	1977	59	10	7	3	26	21	36	50	58	7	4	7														
Er		2112	215	690	199	1072	6504	201	46	33	16	87	68	121	173	189	34	21	30														
Tm		395	33	137	35	132	830	31	9	6	3	14	11	22	30	34	8	4	5														
Yb		3045	262	1166	297	1014	5720	238	90	54	31	110	88	187	237	286	76	43	52														
Lu		499	46	213	60	303	1261	44	18	11	6	20	15	31	41	48	17	9	10														
Pt		49.8	57.0	29.4	12.7	39.7	14.2	10.9	17.7	17.3	15.5	28.1	18.3	16.5	27.2	18.2	19.3	9.7	8.2														
Pd		38.8	50.0	48.3	4.4	36.4	17.3	8.9	16.6	12.9	21.6	18.4	10.5	14.8	15.5	13.8	22.1	8.1	7.2														
Total (wt%)		101.5	100.1	98.5	101.1	98.7	98.7	99.1	98.7	99.4	99.5	101.8	100.3	100.3	101.0	99.4	97.4	97.7	99.0														
ΣREE (ppm)		53	14	18	2	59	139	4	1	8	0.1	4	3	3	11	7	0.2	0.2	0.2														
Pt+Pd (ppb)		88.6	107	77.7	17.1	76.1	31.5	19.8	34.3	30.2	37.1	46.5	28.8	31.3	42.7	32.0	41.4	17.8	15.4														
UMIA%		90	70	84	47	78	36	25	8	5	3	92	93	91	91	86	7	5	3														
pH		6.05	5.87	5.98	6.50	5.33	5.28	7.65	8.68	8.94	n.a.	5.92	5.98	5.58	5.38	5.70	8.08	8.20	n.a.														
τ _{Ti,Si}		-0.99	-0.94	-0.98	-0.92	-0.96	-0.74	-0.66	-0.78	0.02	0	-0.99	-1.00	-0.99	-0.99	-0.97	0.52	2.82	0														
τ _{Ti,Al}		1.04	1.07	0.43	0.69	0.72	0.00	0.54	-0.29	0.56	0	0.81	0.82	2.12	2.64	2.76	1.46	1.12	0														
τ _{Ti,Fe}		1.38	1.82	1.53	0.39	1.11	0.90	1.30	-0.48	0.45	0	0.60	0.62	2.05	1.84	2.53	0.97	1.72	0														
τ _{Ti,Mn}		0.85	1.26	-0.51	0.23	92.1	82.3	0.19	1.78	0.15	0	-0.44	-0.66	-0.54	3.35	-0.60	1.12	1.69	0														
τ _{Ti,Mg}		-1.00	-0.98	-0.99	-0.96	-1.00	-0.99	-0.86	-0.83	-0.19	0	-1.00	-1.00	-0.99	-0.99	-0.99	-0.34	-0.67	0														
τ _{Ti,Ca}		-1.00	-	-1.00	-0.89	-0.99	-0.99	-0.99	-0.74	-0.74	0	-1.00	-1.00	-1.00	-1.00	-1.00	0.39	-0.50	0														
τ _{Ti,Na}		3.31	4.62	3.68	1.92	5.61	6.47	4.68	0.25	3.17	0	1.35	1.36	3.36	3.19	4.37	8.82	27.9	0														
τ _{Ti,K}		-0.88	-	-	-0.88	0.07	-0.43	-0.38	-0.79	-0.13	0	-0.91	-0.88	-0.78	-	-0.83	0.22	2.59	0														
τ _{Ti,P}		-0.63	-0.59	-0.69	-0.75	-0.54	-0.52	-0.42	-0.80	0.14	0	-0.26	-0.20	-0.47	-0.53	-0.37	0.07	1.15	0														
τ _{Ti,Sc}		2.16	4.79	2.21	2.28	4.55	2.63	0.76	0.78	2.67	0	0.04	-0.02	1.01	1.32	1.24	1.33	0.84	0														
τ _{Ti,V}		0.26	1.06	0.38	0.11	0.43	0.04	0.33	-0.52	0.48	0	0.35	0.41	1.39	1.65	1.95	1.94	1.57	0														
τ _{Ti,Cr}		0.85	2.15	2.59	0.63	0.66	0.93	1.71	-0.51	0.92	0	0.48	0.86	1.61	1.17	1.70	1.86	1.73	0														
τ _{Ti,Co}		0.29	0.91	0.75	0.23	32.2	18.2	1.02	-0.29	9.94	0	-0.54	-0.77	0.22	3.89	-0.17	0.96	1.84	0														
τ _{Ti,Ni}		0.54	2.82	1.07	0.87	0.98	0.54	3.68	0.50	9.41	0	0.11	-0.17	2.11	1.91	3.27	2.30	2.78	0														
τ _{Ti,Cu}		-0.11	-0.24	-0.39	-0.75	-0.13	-0.35	-0.68	-0.95	-	0	-0.59	-0.67	-0.31	-0.36	-0.28	0.19	-0.70	0														
τ _{Ti,Zn}		2.02	4.18	3.17	1.50	6.89	1.94	2.61	-0.14	7.93	0	0.42	0.22	1.54	1.70	2.26	0.37	0.91	0														
τ _{Ti,ΣREE}		131	44.5	48.2	3.46	222	583	17.7	0.98	85.5	0	3.54	2.18	5.00	24.9	19.0	0.81	2.26	0														
τ _{Ti,Pt+Pd}		-0.35	0.06	-0.36	-0.90	-0.15	-0.61	-0.73	-0.77	-0.08	0	-0.42	-0.63	-0.23	0.01	-0.06	2.38	1.70	0														

(Continues)

TABLE 1 (Continued)

Mining area		Soroako										Pomalaa									
Hill		Petee										Willson									
Sample name		20-18	20-19	20-20	20-21	20-22	20-23	20-24	20-25	20-26-1	22_1	22_2	22_3	22_4	22_5	22_6	22_7	22_8			
Sample type		RL	YL	YL	YL	MO	Sa	Sa	Sa	BR	RL	RL	YL	Sa	Sa	Sa	BR				
Depth (m)		0.6	5.5	7.5	11	17.5	19.5	25.3	28.9	32	1.5	4.5	8.5	10.5	15.7	20	23.5	26.7			
Wt%																					
SiO ₂	4.11	8.49	2.24	2.74	4.28	36.9	34.3	34.3	39.1	40.3	1.90	8.35	18.2	32.8	45.1	44.6	45.0	39.6			
Al ₂ O ₃	10.3	6.28	8.14	3.26	5.12	2.17	1.14	1.14	5.20	0.92	8.00	6.06	5.48	3.04	0.88	1.38	1.36	0.64			
Fe ₂ O ₃	64.5	62.9	68.6	75.8	61.6	19.4	25.0	25.0	14.0	7.96	70.1	63.0	51.7	33.6	10.5	16.1	15.1	8.27			
MnO	0.44	1.44	0.88	0.34	7.43	0.44	0.36	0.36	0.23	0.11	0.25	1.00	2.51	0.95	0.15	0.23	0.20	0.12			
MgO	0.80	0.89	0.64	0.35	1.05	21.0	18.9	18.9	23.6	38.2	0.47	0.63	3.10	13.3	28.9	22.2	21.6	36.2			
CaO	0.040	0.010	0.008	0.009	0.016	0.118	0.123	0.123	0.328	1.124	0.011	0.009	0.012	0.076	0.713	0.670	0.711	0.555			
Na ₂ O	0.17	0.18	0.18	0.19	0.16	0.09	0.09	0.09	0.10	0.02	0.17	0.18	0.19	0.14	0.05	0.08	0.09	0.02			
K ₂ O	0.005	<0.004	<0.004	0.004	<0.004	0.008	0.006	0.006	0.009	0.007	0.005	0.004	<0.004	<0.004	0.005	0.007	0.004	0.008			
TiO ₂	0.29	0.09	0.11	0.02	0.04	0.03	0.02	0.02	0.06	0.03	0.12	0.04	0.03	0.03	0.03	0.03	0.01	0.01			
P ₂ O ₅	0.020	0.011	0.010	0.009	0.007	0.007	0.007	0.007	0.006	0.007	0.020	0.012	0.011	0.008	0.006	0.006	0.006	0.002			
Cr ₂ O ₃	2.64	2.36	2.63	1.53	2.61	1.01	0.80	0.80	0.67	0.37	2.96	3.11	2.58	1.74	0.46	0.83	0.84	0.33			
CoO	0.087	0.220	0.111	0.078	0.737	0.053	0.043	0.043	0.023	0.013	0.042	0.114	0.266	0.120	0.017	0.028	0.025	0.014			
NiO	1.09	1.95	2.09	3.17	3.99	3.53	4.65	4.65	2.87	0.26	2.09	3.18	3.07	3.77	0.39	2.17	1.92	0.28			
LOI	15.2	13.5	15.2	13.9	14.2	14.0	12.9	12.9	13.6	10.7	14.6	13.8	12.1	11.3	12.7	11.4	12.4	12.1			
ppm																					
Sc	59	52	81	36	46	13	16	16	32	15	71	65	56	42	10	22	17	13			
V	287	216	300	192	192	87	74	74	99	51	319	218	246	150	55	81	87	41			
Cr	18071	16150	17970	10450	17877	6939	5459	5459	4558	2555	20234	21255	17634	11911	3143	5670	5781	2269			
Co	686	1727	876	612	5793	415	341	341	180	106	334	897	2094	945	132	221	198	109			
Ni	8593	15301	16420	24914	31365	27737	36566	36566	22543	2063	16395	24977	24141	29661	3103	17088	15077	2225			
Cu	245	239	358	241	140	<1.6	<1.6	<1.6	41	52	255	183	218	24	4	<1.6	<1.6	16			
Zn	403	452	709	676	422	136	135	135	67	34	371	622	708	803	53	100	117	42			
ppb																					
La	755	1555	856	1664	1735	248	16	16	78	2	1284	3592	7318	14043	20	538	677	12			
Ce	3444	664	4582	269	8053	420	32	32	132	7	2811	5098	41761	10434	51	27	18	78			
Pr	241	1214	331	521	656	58	6	6	21	1	295	549	1865	2623	5	108	20	2			
Nd	1106	6351	1375	2050	2851	258	29	29	97	2	1068	1882	7527	9647	13	437	55	4			
Sm	359	2025	389	209	716	73	13	13	37	1	202	314	1884	1598	2	57	1	b.d.			
Eu	110	528	87	51	174	27	5	5	20	b.d.	41	62	384	326	0.5	13	0.4	b.d.			
Gd	435	1827	352	482	717	112	29	29	74	6	191	269	1526	1736	5	64	6	2			
Tb	83	366	65	66	126	23	7	7	19	3	34	41	250	245	1	9	2	1			

TABLE 1 (Continued)

Dy	582	2417	427	538	835	184	64	149	27	233	259	1605	1565	13	65	18	9
Ho	122	483	92	153	182	45	18	36	8	51	54	323	357	4	18	7	3
Er	385	1513	304	532	600	157	68	127	38	170	179	1129	1157	23	70	34	17
Tm	61	261	51	70	99	26	12	21	7	29	30	207	168	5	12	8	3
Yb	446	1866	391	480	756	204	104	165	66	221	236	1661	1194	51	107	77	37
Lu	72	297	65	103	131	37	20	29	13	39	41	286	216	10	21	17	8
Pt	14.3	45.3	9.9	20.0	37.0	16.4	11.5	9.5	2.4	31.2	31.9	39.0	23.9	10.8	15.5	16.5	8.3
Pd	10.1	39.9	7.5	17.9	36.6	14.2	6.5	9.7	2.1	13.6	17.4	36.3	25.1	9.3	13.4	14.2	7.1
Total (wt%)	99.9	98.4	101.1	101.6	101.4	98.8	98.5	98.8	100.1	100.9	99.6	99.5	101.0	99.9	99.9	99.3	98.1
ΣREE (ppm)	8	21	9	7	18	2	0.4	1	0.2	7	13	68	45	0.2	2	1	0.2
Pt+Pd (ppb)	24.4	85.2	17.4	37.9	73.6	30.6	18.0	19.2	4.5	44.8	49.3	75.3	49.0	20.1	28.9	30.7	15.4
UMIA%	85	74	91	90	82	11	14	10	4	92	75	50	22	5	8	8	4
pH	6.14	5.56	5.34	5.34	5.58	7.90	8.05	8.17	n.a.	5.30	5.19	5.97	7.05	8.72	8.20	8.16	n.a.
$\epsilon_{\text{Tl,SI}}$	-0.99	-0.94	-0.99	-0.93	-0.94	-0.24	0.11	-0.56	0	-1.00	-0.95	-0.79	-0.63	-0.50	-0.58	-0.07	0
$\epsilon_{\text{Tl,Al}}$	-0.05	0.98	1.08	2.53	2.11	0.95	0.61	1.54	0	0.24	1.47	2.85	1.11	-0.40	-0.20	0.74	0
$\epsilon_{\text{Tl,Fe}}$	-0.31	1.31	1.03	8.54	3.34	1.02	3.11	-0.20	0	-0.16	0.98	1.81	0.81	-0.45	-0.28	0.49	0
$\epsilon_{\text{Tl,Mn}}$	-0.67	2.68	0.81	1.99	35.4	2.17	3.13	-0.08	0	-0.78	1.25	8.76	2.65	-0.44	-0.27	0.43	0
$\epsilon_{\text{Tl,Mg}}$	-1.00	-0.99	-1.00	-0.99	-0.98	-0.54	-0.35	-0.72	0	-1.00	-1.00	-0.96	-0.84	-0.65	-0.77	-0.51	0
$\epsilon_{\text{Tl,Ca}}$	-1.00	-1.00	-1.00	-0.99	-0.99	-0.91	-0.86	-0.87	0	-1.00	-1.00	-0.99	-0.94	-0.44	-0.55	0.05	0
$\epsilon_{\text{Tl,Na}}$	-0.29	1.59	1.06	8.03	3.47	2.69	4.98	1.17	0	-0.24	1.09	2.87	1.83	0.04	0.40	2.19	0
$\epsilon_{\text{Tl,K}}$	-0.94	-	-	-0.40	-	-0.10	0.11	-0.45	0	-0.94	-0.86	-1.00	-0.85	-0.71	-0.67	-0.64	0
$\epsilon_{\text{Tl,P}}$	-0.76	-0.54	-0.66	0.21	-0.46	-0.20	0.27	-0.62	0	0.16	0.78	1.91	1.02	0.52	0.30	1.84	0
$\epsilon_{\text{Tl,Sc}}$	-0.67	0.02	0.28	1.44	0.74	-0.29	0.38	-0.04	0	-0.44	0.35	0.98	0.48	-0.65	-0.35	0.11	0
$\epsilon_{\text{Tl,V}}$	-0.52	0.25	0.40	2.79	1.12	0.43	0.91	-0.12	0	-0.22	0.40	1.72	0.64	-0.41	-0.26	0.76	0
$\epsilon_{\text{Tl,Cr}}$	-0.40	0.84	0.66	3.10	2.92	1.25	1.79	-0.19	0	-0.12	1.44	2.49	1.33	-0.40	-0.08	1.08	0
$\epsilon_{\text{Tl,Co}}$	-0.45	3.76	0.95	4.78	29.6	2.26	3.20	-0.23	0	-0.70	1.14	7.61	2.84	-0.47	-0.25	0.48	0
$\epsilon_{\text{Tl,Ni}}$	-0.65	1.16	0.88	11.1	7.52	10.2	22.1	3.94	0	-0.27	1.92	3.87	4.92	-0.39	1.83	4.53	0
$\epsilon_{\text{Tl,Cu}}$	-0.60	0.35	0.63	3.68	0.52	-	-	-0.64	0	0.59	2.00	5.17	-0.32	-0.89	-	-	0
$\epsilon_{\text{Tl,Zn}}$	-0.01	2.83	3.85	18.6	5.86	2.27	4.12	-0.12	0	-0.12	2.86	6.58	7.50	-0.45	-0.12	1.27	0
$\epsilon_{\text{Tl,ΣREE}}$	2.83	33.4	11.2	38.7	53.5	7.58	2.04	1.51	0	2.78	17.7	172	114	-0.49	2.25	3.38	0
$\epsilon_{\text{Tl,Pt+Pd}}$	-0.54	4.52	-0.09	7.44	8.17	4.65	4.22	0.93	0	-0.71	-0.17	1.19	0.41	-0.43	-0.31	0.63	0

Note: -, not calculated because concentration of mobile element is below detection limit.

Abbreviations: b.d., below detection limit; n.a., not analyzed; LOI, loss on ignition; UMIA, ultramafic index of alteration; RL, red laterite; YL, yellow laterite; MO, Mn-oxide; Sa, saprolite; BR, bedrock.

index, namely, the ultramafic index of alteration (UMIA), which was modified for ultramafic rock by Aiglsperger *et al.* (2016) following work by Babechuk *et al.* (2014), was calculated using Equation (1) and expressed in molar ratios:

$$\text{UMIA} (\%) = \left[\frac{(\text{Al}_2\text{O}_3 + \text{Fe}_2\text{O}_{3[\text{T}]})}{(\text{SiO}_2 + \text{MgO} + \text{Al}_2\text{O}_3 + \text{Fe}_2\text{O}_{3[\text{T}]})} \right] \times 100. \quad (1)$$

The relative loss or gain of elements during chemical weathering was measured using the element mass transfer coefficient, τ_{ij} , which represents changes in ratios of elements to immobile elements, relative to bedrock, and is calculated as follows (e.g., Brimhall and Dietrich, 1987):

$$\tau_{ij} = \frac{C_{j,w}C_{i,p}}{C_{j,p}C_{i,w}} - 1 \quad (2)$$

where C_j is the content of element j (wt%), and C_i is the content of immobile element i (wt%). The subscripts w and p refer to weathered material and bedrock, respectively. Titanium (Ti) was used as the immobile element for the calculation of τ_{ij} . Positive or negative τ_{ij} values denote the external addition or loss of element j relative to bedrock, respectively. If $\tau_{ij} = 0$, then element j is neither enriched nor depleted, and if $\tau_{ij} = -1$, then element j has been completely removed from the weathering profile.

The total mass of a lost or added to the weathered profile per unit landscape area for a mobile element ΔM_j (kg/m²) was obtained for the studied profiles and also for previously reported laterite profiles from other tropical regions (West Block and Petea Block, Indonesia: Sufriadin *et al.*, 2011; Kolonodale, Indonesia: Fu *et al.*, 2014; Punta Gorda, Cuba, and Loma Caribe and Loma Peguera, Dominican Republic: Aiglsperger *et al.*, 2016; Tagaung Taung, Myanmar: Schellmann, 1989) by integrating τ_{ij} over the regolith thickness (Chadwick *et al.*, 1990):

$$\Delta M_j (\text{kg/m}^2) = \Sigma C_{j,p} \rho_p \tau_{ij} D \quad (3)$$

where $C_{j,p}$ is the content of the mobile element of bedrock (kg/ton), ρ_p is the density of bedrock (ton/m³), τ_{ij} is the element mass transfer coefficient, and D (m) is the distance between upper and lower samples. For bedrock density, the values of 2.85 and 2.35 ton/m³ reported by Sufriadin *et al.* (2011) for harzburgite and serpentinized harzburgite collected from West Block and Petea Block were used for fresh peridotite and serpentinized peridotite, respectively.

4 | RESULTS

4.1 | Porewater pH and whole-rock geochemistry

The pH values of the laterite samples from all of the studied profiles fall in the range of 5.19–8.94, with the highest value in the saprolite horizon and the lowest in the red laterite horizon (Table 1). The pH varies from higher values in the saprolite horizon (7.05–8.94) to lower values in the oxide zone (5.19–6.14), indicating that the soil environment changes from slightly alkaline to acidic toward the surface.

The major, minor, and critical metal contents for the studied profiles are given in Table 1. Figures 3 and 4 show the vertical distributions of selected major element (MgO, SiO₂, Fe₂O₃, Al₂O₃, and Cr₂O₃), minor element (NiO, CoO, and MnO), and critical metal (Sc, REEs, Pt, and Pd) contents for two representative laterite profiles, Konde and Petea hills. At Konde Hill, which is developed on harzburgite, bedrock is dominated by Mg (43.6 wt% MgO) and Si (43.2 wt% SiO₂), which show an abrupt decrease at the transition boundary between the saprolite horizon and oxide zone (<1.19 wt% MgO, <2.86 wt% SiO₂), whereas upward enrichment is observed for Fe, Al, and Cr, up to 73.4 wt% Fe₂O₃, 7.68 wt% Al₂O₃, and 4.24 wt% Cr₂O₃ (Figure 3). Among the studied profiles, Konde Hill shows a marked increase in SiO₂ content from 52.2 to 70.5 wt% in the saprolite horizon (Figure 3). Petea Hill, where the bedrock is serpentinized harzburgite, shows similar trends in major elements to those of Konde Hill. The bedrock and saprolite at Petea Hill contain 18.9–38.2 wt% MgO and 34.3–40.3 wt% SiO₂, whereas the oxide zone contains <1.05 wt% MgO and <8.49 wt% SiO₂. This geochemical difference is coupled with increases in Fe₂O₃, Al₂O₃, and Cr₂O₃ contents from 7.96, 0.92, and 0.37 wt% in bedrock up to 75.8, 10.3, and 2.64 wt% at the top of the profile, respectively (Figure 4). The Watulabu and Willson Hill profiles also show similar trends with respect to major elements, although the variations are less than those for the other two hill profiles (Figures S1 and S2).

The UMIA values are low in bedrock (3–4) and progressively increase from the saprolite horizon (5–25) toward the top of each profile (36–93 in the oxide zone), although local occurrences of quartz in the oxide zone commonly result in low UMIA values, disrupting the general weathering trend (Table 1, Figure 5). Samples from the lower part of the oxide zone at Watulabu and Willson hills (samples 20–4 and 22–3) have lower UMIA values (47 and 50, respectively) than those at Konde and Petea hills (Table 1), suggesting that the profiles of the former are less weathered than those of the latter

FIGURE 3 Vertical profile for Konde Hill, showing contents of major elements, relevant minor elements, and critical metals. RL, red laterite; YL, yellow laterite; Sa, saprolite; BR, bedrock

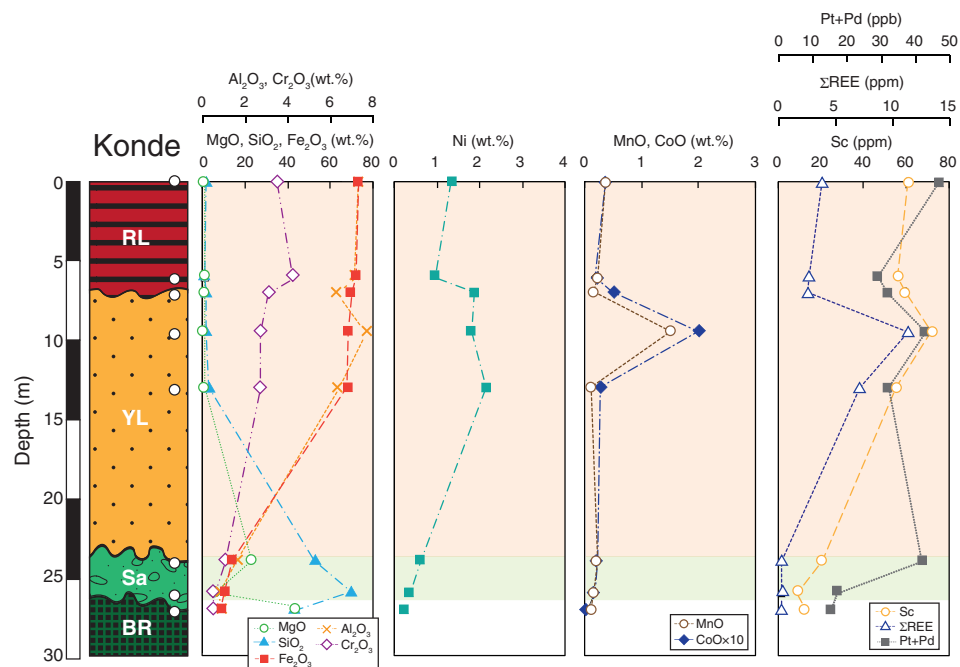
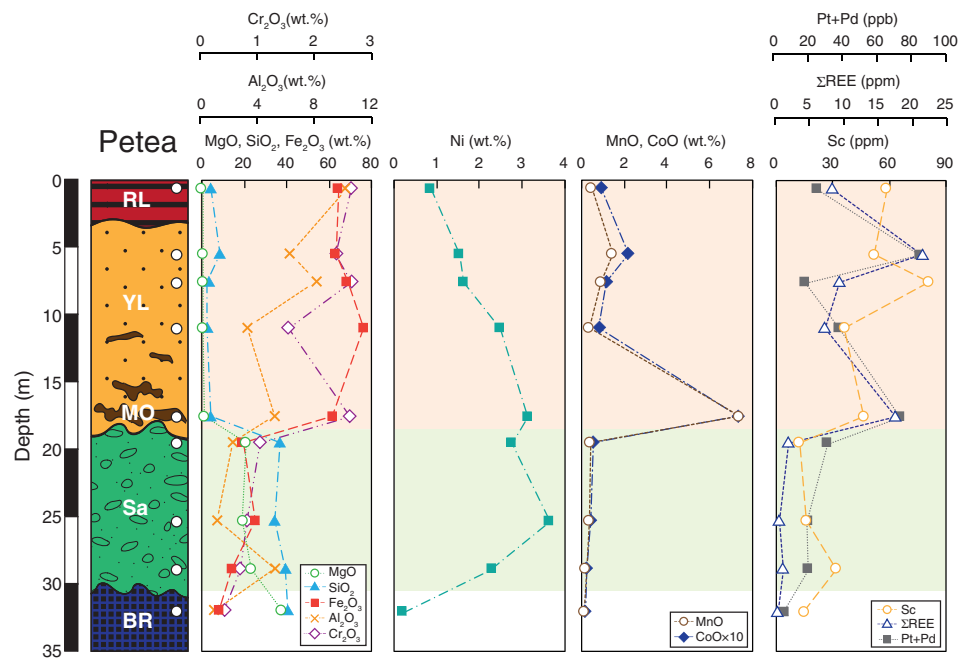


FIGURE 4 Vertical profile for Petea Hill, showing contents of major elements, relevant minor elements, and critical metals. RL, red laterite; YL, yellow laterite; MO, Mn-oxide; Sa, saprolite; BR, bedrock



(i.e., Konde, Petea > Watulabu, Willson). This trend in the degree of weathering is consistent with that predicted from the thicknesses of the weathering profiles (Figure 2a).

Bedrock from the studied profiles shows similar Ni contents of 0.21–0.24 wt% that are consistent with those previously reported for ultramafic rocks from the ESO (Kadarusman *et al.*, 2004). Nickel contents increase from the bedrock toward the top of profiles and show the highest contents in different horizons depending on profile location. At Petea and Willson hills, the saprolite

horizons show the highest Ni contents, up to 3.66 and 2.97 wt% with mean values of 2.89 and 2.06 wt%, respectively (Figure 4 and Figure S2). In contrast, the saprolite horizons of Watulabu and Konde hills have lower mean Ni contents of 1.92 and 0.48 wt%, respectively. The oxide zones show fairly homogeneous Ni contents at all hills compared with the saprolite horizons, with mean values ranging from 1.55 to 2.18 wt%. At Petea Hill, the content of Ni gradually decreases toward the top of the profile, whereas in the other profiles it decreases in the uppermost horizon (Figure 3 and Figure S1).

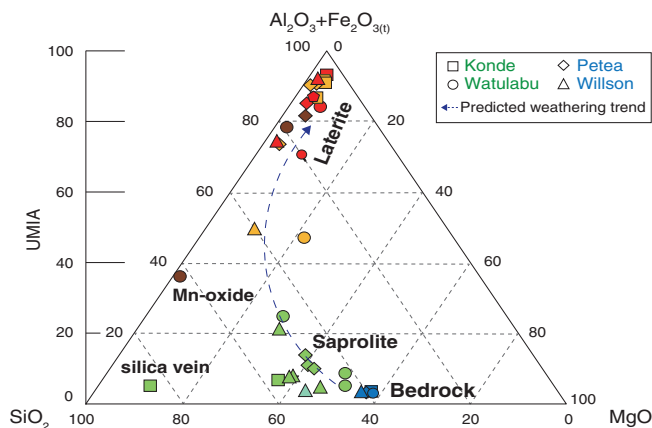


FIGURE 5 Molar ternary plot of (Al + Fe)-Si-mg space showing the weathering trends of ultramafic rocks and their relationships with UMIA for Watulabu Hill (circles), Konde Hill (squares), Petea Hill (diamonds), and Willson Hill (triangles). Color coding: Red laterite (red), yellow laterite (yellow), Mn-oxide (brown), saprolite (green), and bedrock (blue). The dashed blue line with arrow shows the predicted weathering trend with initial loss of MgO followed by loss of SiO₂ and subsequent enrichment of Al₂O₃ and Fe₂O₃

Mn shows marked enrichment in the Mn-oxide horizons at Watulabu and Petea hills, with up to 28.7 and 7.43 wt% MnO, respectively, contrasting with a mean MnO content of 0.12 wt% in the bedrock (Figure 4 and Figure S1). Co contents are low in the bedrock (mean 0.014 wt% CoO), are positively correlated with Mn, and reach up to 1.20 and 0.74 wt% in the Mn-oxide horizon of the two profiles. These two elements do not show marked enrichment in other horizons. At Konde and Willson hills, the contents of Mn and Co show similar trends with depth, although the highest contents observed in the yellow laterite sub-horizons are one order of magnitude lower (1.51 and 2.51 wt% MnO, 0.20 and 0.27 wt% CoO) compared with Watulabu and Petea hills (Figure 3 and Figure S2).

The Sc content of bedrock ranges from 3 to 15 ppm and is positively correlated with Al₂O₃ and CaO contents (Table 1). In the saprolite horizons, Sc contents increase from 10 to 42 ppm. In all studied profiles, Sc is enriched in the oxide zone compared with the bedrock, ranging from 24 to 81 ppm, with mean contents of 38–64 ppm. These Sc contents further increase in the oxide zone from 24 to 81 ppm, with mean contents of 38 to 64 ppm. The highest contents are in the range 49–81 ppm (Figures 3 and 4) and are positively related to Sc contents of the bedrock. The vertical distribution of REEs is highly correlated with those of Mn and Co in the studied profiles (Figures 3 and 4). REE contents show substantial enrichment, reaching up to 11–139 ppm in Mn-oxide horizons, contrasting with low contents of 0.1–0.2 ppm in bedrocks.

The highest REE content among the studied hills is observed in the lower Mn-oxide horizon of Watulabu Hill (139 ppm), and the Mn-enriched sample from the oxide zone of Willson Hill shows a higher REE content (68 ppm) than those of Konde (11 ppm) and Petea (21 ppm). The enrichments in REEs, unlike Sc, show no clear correlations with bedrock contents. Pd + Pt contents vary from 4.5 to 37.1 ppb in the bedrock, with the lowest value at Petea Hill and the highest at Watulabu Hill (Table 1). The bedrock of both Konde and Willson hills shows Pd + Pt contents of 15.4 ppb, intermediate between those of the other two hills. Pd + Pt contents generally show a residual enrichment pattern, with higher values in the oxide zone with respect to those in saprolite horizon and bedrock, similar to that observed for Sc (Figures 3 and 4). The highest contents are observed at the top of profiles or below the top where Mn is enriched. Among the studied profiles, the mean contents of Pd + Pt in the oxide zones are 36–66 ppb, with the highest contents ranging from 47 to 107 ppb. At Petea Hill, Pd + Pt contents are enriched up to about 19 times higher than those in the bedrock, whereas the other hills show enrichments of 3–5 times relative to bedrock (Table 1).

4.2 | Mass-balance calculations

The calculation results for τ_{ij} and the patterns from bedrock to the top of the two representative laterite profiles, Petea and Konde hills, are presented in Table 1 and Figures 6 and 7. The total mass losses and gains through the studied profiles and previously investigated profiles are given in Table S1. Mg and Si are continuously lost upward through the profiles, with marked loss shown in saprolite (up to $\tau_{\text{Ti,Mg}} = -0.86$, $\tau_{\text{Ti,Si}} = -0.78$) then these elements are completely lost ($\tau_{ij} = -1$) at the top of the profile for all of the studied hills, except for the lower saprolite horizons of Konde Hill, which show large gains in Si ($\tau_{\text{Ti,Si}}$ up to +2.82) (Figure 6). Other major elements, such as Ca and K, also show patterns of marked loss from the bedrock to the top (surface). These values correspond to mean mass transfers of $-6,215 \text{ kg/m}^2$ Si, $-11,014 \text{ kg/m}^2$ Mg, and -268 kg/m^2 Ca in the studied profiles.

In contrast, the τ values of Fe, Al, and Cr show increases from the bedrock toward the surface of the profiles and have similar ranges ($\tau_{\text{Ti,Fe}} = -0.48$ to +2.53, $\tau_{\text{Ti,Al}} = -0.42$ to +2.85, $\tau_{\text{Ti,Cr}} = -0.51$ to +3.10), except for the $\tau_{\text{Ti,Fe}}$ values of Petea Hill. Petea Hill shows a greater gain in Fe up through the profile than those of the other hills, reaching up to +3.11 in the saprolite horizon and +8.54 in the yellow laterite sub-horizon (Figure 7). In the red laterite sub-horizon of Watulabu and Konde hills, Fe

FIGURE 6 Vertical distribution of the mass transfer coefficient (τ) of major elements, relevant minor elements, and critical metals in the Ni laterite profile of Konde Hill. Vertical lines show zero positions with respect to the calculations of τ . RL, red laterite; YL, yellow laterite; Sa, saprolite; BR, bedrock

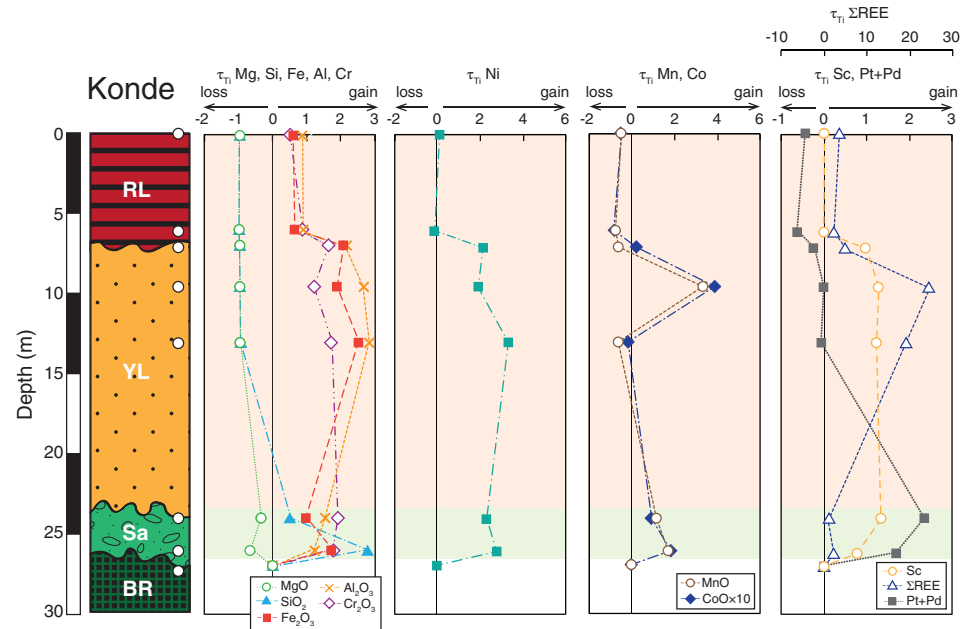
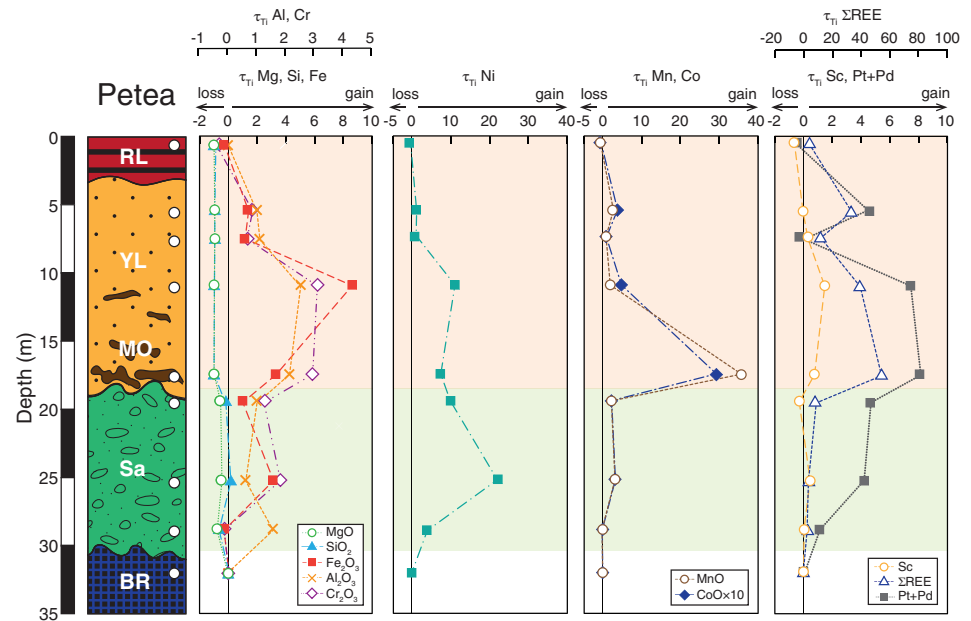


FIGURE 7 Vertical distribution of the mass transfer coefficient (τ) of major elements, relevant minor elements, and critical metals for the Ni laterite profile of Petea Hill. Vertical lines show zero positions with respect to the calculations of τ . RL, red laterite; YL, yellow laterite; MO, Mn-oxide; Sa, saprolite; BR, bedrock



shows mass gains of +1.38 and +0.6, respectively (Figure 6 and Figure S3), whereas at Petea and Willson hills the red laterite sub-horizon displays a mass loss in Fe (−0.31 and −0.16, respectively) (Figure 7 and Figure S4). The order of total mass transfers of Fe upward through the profiles is as follows: Petea (+10,647 kg/m²) > Konde (+6,955 kg/m²) > Watulabu (+1,473 kg/m²) > Willson (+1,349 kg/m²). The pronounced mass gain for Petea Hill is the highest value among the calculated values, including the studied profiles and previously investigated Ni

laterite profiles in tropical regions, which range from −631 to +6,177 kg/m² (Table S1).

Nickel shows wide ranges of gain upward through the weathering profiles, particularly in the saprolite horizon. The saprolite horizon of Petea Hill shows an extreme gain in Ni (τ_{Ni} = +3.94 to +22.1) (Figure 7), whereas the other hills have moderate gains with a range of τ_{Ni} from +0.50 to +4.92, except for a low τ_{Ni} value of −0.39 in the upper part of the saprolite at Willson Hill and a value of +9.41 in the lower part of

the saprolite at Watulabu Hill (Figures S3 and S4). The oxide zone also shows gains in Ni, with similar mean $\tau_{\text{Ti,Ni}}$ values ranging from +1.14 to +1.84 in the profiles at Watulabu, Konde, and Willson hills, and Petea Hill having a mean $\tau_{\text{Ti,Ni}}$ of +4.00. The red laterite sub-horizon shows losses in Ni, with $\tau_{\text{Ti,Ni}}$ values of −0.65 and −0.27 at Petea and Willson hills, respectively, whereas the other two hills show positive $\tau_{\text{Ti,Ni}}$ values (Figure 7 and Figure S4). Ni shows the highest total mass gains next to those of Fe for the studied profiles (+90 to +1,208 kg/m²), and these values increase with increasing Fe content. Petea Hill shows the highest total mass gain of Ni (+1,208 kg/m²) of the studied profiles and other Ni laterite profiles in tropical regions (+27 to +1,137 kg/m²) (Table S1).

The mass transfer coefficients for Co ($\tau_{\text{Ti,Co}}$) and Mn ($\tau_{\text{Ti,Mn}}$) show wide-ranging values (Figures 6 and 7), with substantial gains ranging from +3.89 to +32.2 and from +1.84 to +92.1 in the lower part of the oxide zone, respectively. The highest τ values for both Co and Mn are observed in the Mn-oxide horizon of Watulabu Hill. With respect to the total mass gain, Petea Hill shows the highest values for Co (+47 kg/m²) and Mn (+402 kg/m²), followed by Watulabu Hill (Co = +14 kg/m², Mn = +304 kg/m²). Konde and Willson hills show smaller total mass gains in Co (+5 to +9 kg/m²) and Mn (+29 to +78 kg/m²) compared with the other two hills.

Sc shows a similar distribution pattern of τ to that of Fe in the studied profiles. This element shows low to moderate gains upward from the saprolite horizon (up to $\tau_{\text{Ti,Sc}} = +0.48$) to the oxide zone (up to $\tau_{\text{Ti,Sc}} = +1.44$), with the highest $\tau_{\text{Ti,Sc}}$ values at Petea and Willson hills being in the yellow laterite sub-horizon (Figure 7 and Figure S4). Contrary, Konde and Watulabu hills show Sc gains both in the saprolite horizon and oxide zone (Figure 6 and Figure S3). Higher $\tau_{\text{Ti,Sc}}$ are observed in Watulabu Hill (up to $\tau_{\text{Ti,Sc}} = +2.67$ in saprolite horizon, up to $\tau_{\text{Ti,Sc}} = +4.79$ in oxide zone) than those in other hills. The values of $\tau_{\text{Ti,Sc}}$ are negative in the red laterite sub-horizon or at the top of profiles of Konde, Petea, and Willson hills, ranging from −0.67 to −0.02, whereas Watulabu Hill shows a consistent gain of Sc upward through the profile. REEs generally show a similar vertical pattern of τ to those of Mn and Co, and show an extreme gain in the Mn-oxide horizon or lower part of the oxide zone ($\tau_{\text{Ti,REE}} = +24.9$ to +583), where Mn and Co are also enriched. The highest gain in REEs is observed in the Mn-oxide horizon of Watulabu Hill. In contrast, Pt + Pd show losses throughout the laterite profiles, except for Petea Hill and a few samples from Konde and Willson hills. At Petea and Willson hills, $\tau_{\text{Ti,Pt + Pd}}$ values increase from the lower part of the saprolite horizon upward to the bottom of the oxide zone (+0.93 to

+8.17 and −0.31 to +1.19, respectively), from where they decrease to near the surface (to −0.54 and −0.71, respectively) (Figure 7 and Figure S4).

4.3 | Profile mineralogy

Powder X-ray diffractograms of selected representative samples from different horizons at Konde and Petea hills are shown in Figure 8. Figure 9 shows a summary of the mineralogy for each studied profile based on identification by XRPD, as well as SEM-EDS analyses of thin sections.

Bedrock at Watulabu and Konde hills is dominated by olivine, orthopyroxene, and minor clinopyroxene and Cr-spinel (Figure 8a), whereas bedrock at Petea and Willson hills is dominated by serpentine, followed by olivine, orthopyroxene, and minor clinopyroxene, Cr-spinel, and magnetite (Figure 8b). The mineral composition of saprolite horizons varies among the studied profiles, particularly between Watulabu and Konde hills. At Konde Hill, relicts of primary silicate (olivine and orthopyroxene) with secondary quartz are dominant, whereas at Watulabu Hill, the saprolite horizon is dominated by serpentine, olivine, quartz, and goethite. The saprolite horizon of Petea Hill is dominated by serpentine and secondary phases such as smectite and goethite, as well as quartz. Residual pyroxenes and Cr-spinel are also present as minor mineral phases. Smectite is identified by XRPD analysis on the basis of its characteristic peak at 14.6 Å for a normal sample and a swelling peak at 17.1 Å after EG treatment (Figure 8c). Smectite has a pronounced peak in the lower part of the saprolite horizon and decreases toward the middle to upper part of this horizon. The mineral assemblage of the lower part of the saprolite horizon at Willson Hill is overall similar to that at Petea Hill, although goethite is less dominant. The upper part of the saprolite horizon, the Ni-enriched zone, contains mainly serpentine and goethite, with minor smectite, quartz, talc, and maghemite at both Willson and Petea hills.

In contrast to the saprolite horizon, the oxide zone shows a relatively simple mineral assemblage, consisting mostly of goethite in all studied profiles. As for other Fe-rich minerals, hematite is distinguished mainly in the oxide zones of Watulabu and Konde hills, whereas maghemite is found at Petea and Willson hills. Hematite and maghemite are slightly more abundant toward the upper part of the red laterite sub-horizon, whereas goethite is more dominant in the yellow laterite sub-horizon. Gibbsite, Mn-oxyhydroxides (lithiophorite and/or asbolane), and Cr-spinel are present as other oxide minerals in the oxide zone. Locally, talc and quartz are preserved as relicts in the oxide zone. Talc occurs locally

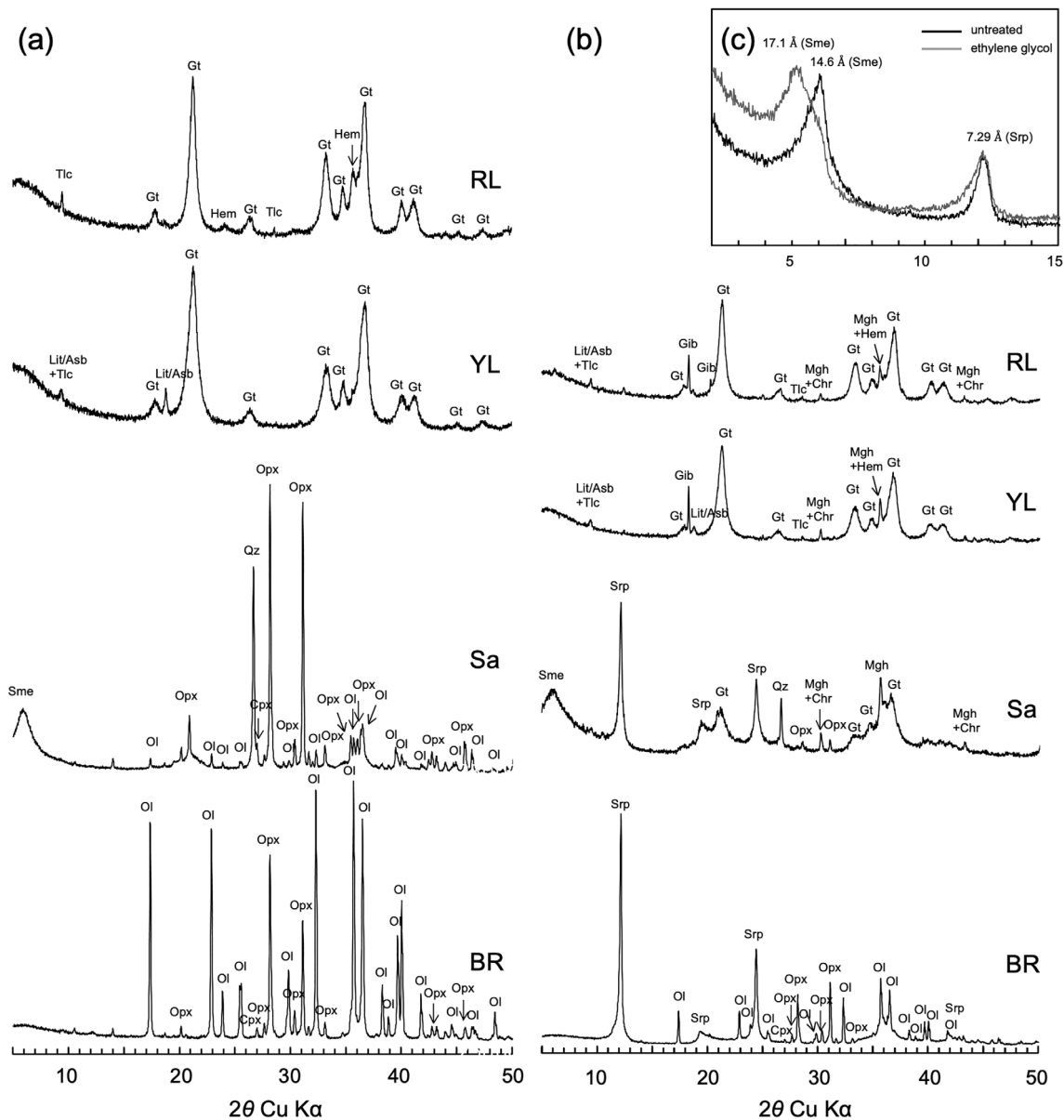


FIGURE 8 Powder X-ray diffractograms of representative samples from the different horizons in the laterite profiles of (a) Konde Hill and (b) Petea Hill, and (c) untreated and glycolated oriented mount X-ray powder diffractograms. RL, red laterite; YL, yellow laterite; Sa, saprolite; BR, bedrock; Hem, hematite; Gt, goethite; Mgh/Chr, maghemite/Cr-spinel; Tlc, talc; Qz, quartz; Lit/Asb, lithiophorite/asbolane; Sme, smectite; Srp, serpentine; Ol, olivine; Opx, orthopyroxene; Cpx, clinopyroxene

through the saprolite horizon to the oxide zone and is more abundant in the latter in the studied profiles. SEM-EDS analyses show that talc has high Mg (mean 29.7 wt% MgO) and Si (mean 60.9 wt% SiO₂) contents and is depleted in Ni. These element contents suggest that talc possibly remains as a residual phase that was originally formed by serpentinization of pyroxene during hydrothermal alteration of the bedrock rather than by replacement of Ni-bearing talc-like minerals (kerolite–pimelite series), although XRPD data and microscope observations show that talc formation is not common in the bedrock. The mineralogy of the studied weathering profiles is

overall similar to that observed in previously investigated Ni laterite profiles in tropical regions (Golightly, 1981; Freyssinet *et al.*, 2005; Butt and Cluzel, 2013 and references therein) and is consistent with the results of Sufriadin *et al.* (2011).

4.4 | Mineral chemistry of Ni-bearing phases

EPMA data for the mineral chemistry of Ni-bearing primary minerals and weathering phases in the bedrock and

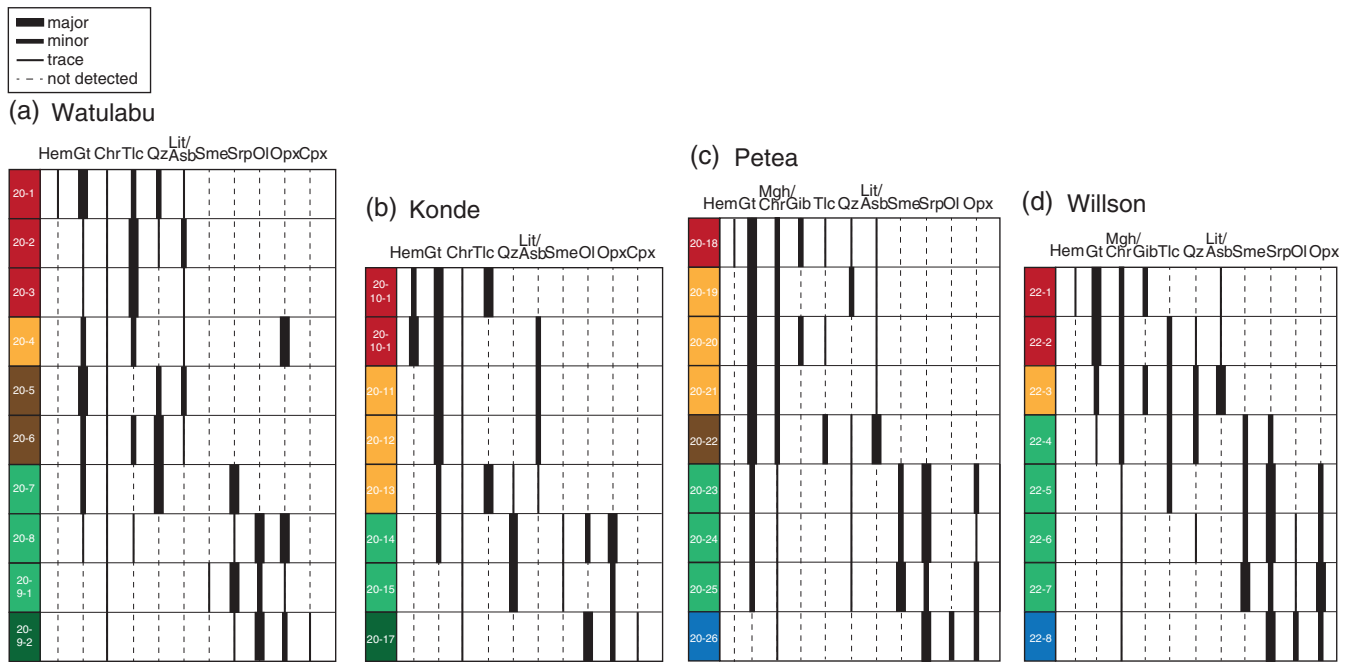


FIGURE 9 Summary of identified mineral compounds of laterite profiles of (a) Watulabu Hill, (b) Konde Hill, (c) Petea Hill, and (d) Willson Hill. Hem, hematite; Gt, goethite; Mgh/Chr, maghemite/Cr-spinel; Tlc, talc; Qz, quartz; Lit/Asb, lithiophorite/asbolane; Sme, smectite; Srp, serpentine; Ol, olivine; Opx, orthopyroxene; Cpx, clinopyroxene. Color coding: Red laterite (red), yellow laterite (yellow), Mn-oxide (brown), saprolite (green), and bedrock (blue)

saprolite horizons of Petea and Willson hills are given in Table S2.

In the bedrock, mean Ni content is highest in olivine (0.36 wt% NiO) and slightly lower in serpentine (0.10 wt%), enstatite (0.10 wt%), and diopside (0.07 wt%). The chemical compositions of these primary silicates are essentially homogeneous between Petea and Willson hills. Primary serpentine found in the bedrock, hereafter referred to as “serpentine I,” has a mesh-like texture surrounding olivine and pyroxenes (Figure 10a,b). In the saprolite horizon, the mesh texture of serpentine is well preserved, although the BSE contrast of surrounding serpentine veins shows the coexistence of different types of serpentine with variable Ni contents. Serpentine with a light-gray color in BSE images has a higher Ni content compared with dark-gray serpentine (Figure 10c,d). On the basis of its higher Ni contents compared with serpentine I, the light-gray serpentine is defined as serpentine II. In the present study, the term “serpentine II” is used for altered primary serpentine (serpentine I) containing higher Ni contents relative to serpentine I and has been described by previous researchers albeit with different terminology (Villanova-de-Benavent *et al.*, 2017; Putzolu *et al.*, 2020). Serpentine II in the sample from the lower part of the saprolite horizon of Petea Hill (sample 20–25) has fairly uniform Ni contents, with a mean value of 3.15 wt% NiO. In contrast, serpentine II in the sample

from the middle part of the saprolite horizon of the same hill (sample 20–24) is characterized by high and variable Ni contents (2.93–10.2 wt%, mean 5.61 wt% NiO), as well as high Fe contents (7.85–14.7 wt% Fe₂O₃). In the middle of the saprolite horizon of Willson Hill, serpentine II shows less enrichment in Ni compared with Petea Hill (sample 22–6; 1.76–4.39 wt%, mean 3.47 wt% NiO), although the Fe contents are similar (7.90–15.6 wt% Fe₂O₃).

In the lower part of the saprolite horizon at Petea Hill, the mesh texture of serpentine is well preserved, although intra-mesh minerals of serpentine, particularly olivine, are progressively replaced by aggregates of fine-grained clay (smectite) (sample 20–25; Figure 10e). These smectites show fairly homogeneous Ni contents, with a mean value of 1.44 wt% of NiO, which is slightly lower than the value for serpentine II. With the progression of weathering, most smectite has been replaced by silicified Fe-(oxy)hydroxide aggregates that have low Ni (<0.12 wt% NiO) in the middle part of the saprolite horizon (Figure 10c,f). The remaining smectite is enriched in Ni, with mean contents of 4.07 wt% NiO for Willson Hill (sample 22–6) and 2.19 wt% NiO for Petea Hill (sample 20–24).

In the oxide zone at both Petea and Willson hills, the original texture has been completely destroyed, and most of the mineral phases observed in the saprolite horizon

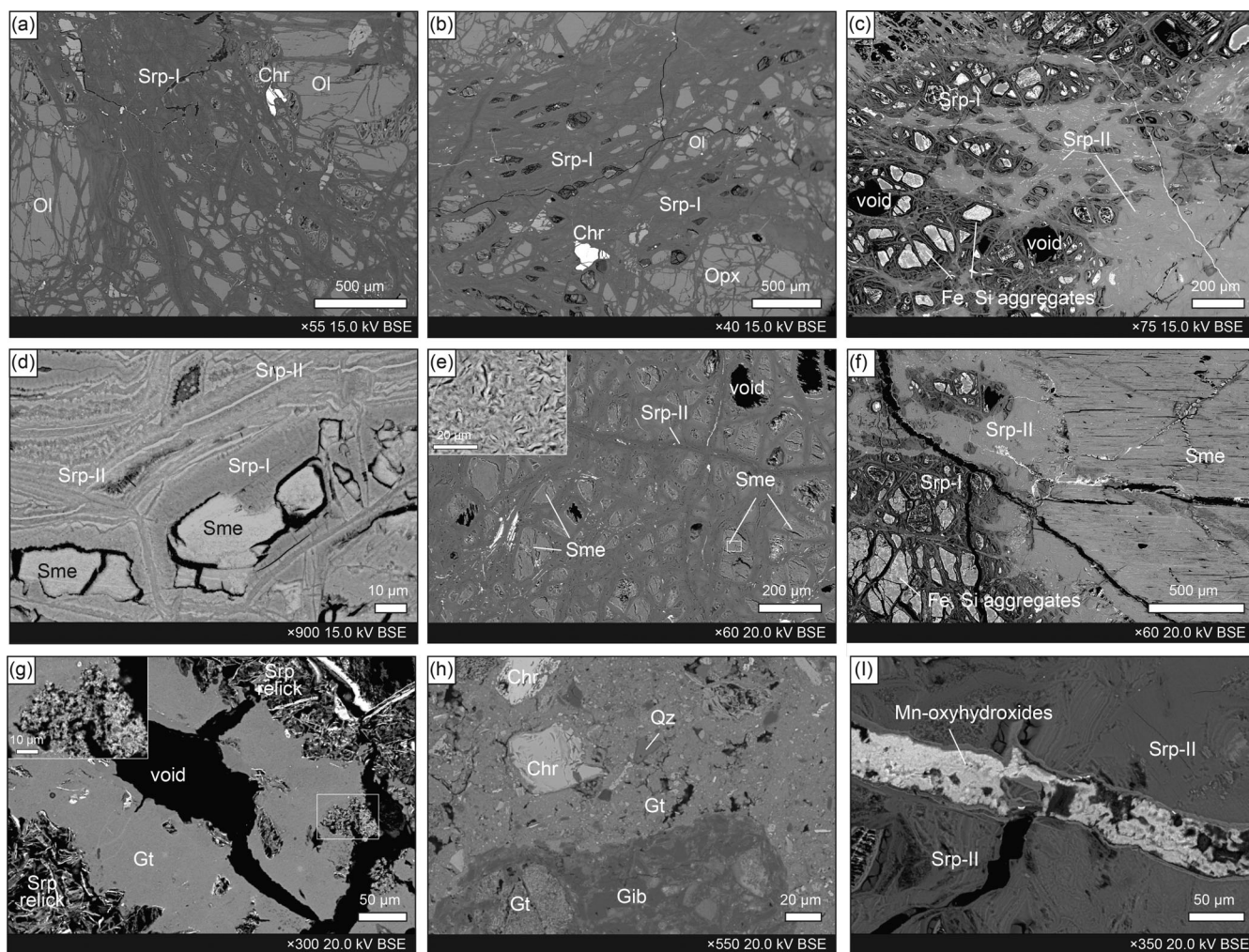


FIGURE 10 SEM images of (a) serpentine I containing low Ni in a bedrock sample (20–26) from Petea Hill, (b) serpentine I with low content of Ni in a bedrock sample (22–8) from Willson Hill, (c) coexistence of low-Ni serpentine I and high-Ni serpentine II, and silicified Fe-(oxy)hydroxide aggregates altered from olivine in a saprolite sample (20–24) from Petea Hill, (d) coexistence of low-Ni serpentine I and high-Ni serpentine II, and aggregates of fine-grained smectite altered from olivine in a sample from the middle part of the saprolite (22–6) from Willson Hill, (e) fine-grained smectite altered from olivine in a sample from the lower part of the saprolite (20–25) from Petea Hill, (f) smectite replacing a large pyroxene grain and surrounding serpentine II in a saprolite sample (20–24) from Petea Hill, (g) aggregates of goethite and a large-scale image of tiny needle-like goethite formed in an open-space relict surrounded by relicts of silicates in a sample of yellow laterite (20–20) from Petea Hill, (h) relicts of Cr-spinel, quartz, gibbsite in goethite matrix in a red laterite sample (20–18) from Petea Hill, and (i) Mn-oxyhydroxides in a saprolite sample (20–24) from Petea Hill

have been replaced by goethite (sample 20–20, 20–18; Figure 10g,h). SEM-EDS analyses show that the goethite matrix has essentially homogeneous Ni contents. The measured Ni contents lie in a narrow range from 1.20 to 1.91 wt% NiO, with a mean content of 1.42 wt% NiO in the yellow laterite sub-horizon at Petea Hill (Figure 10g). Ni contents are slightly lower in the red laterite sub-horizon, ranging from 0.73 to 1.28 wt% NiO, with a mean content of 0.96 wt% NiO (Figure 10h). In the case of Willson Hill, the measured Ni contents of goethite are slightly higher in both the yellow laterite (sample 22–3; 1.06–4.16 wt%, mean 2.73 wt% NiO) and red laterite (sample 22–1; 0.71–3.44 wt%, mean 1.64 wt% NiO) sub-

horizons. Mn-(oxy)hydroxides locally occur as vein fillings along fractures (Figure 10i) and become more abundant in the lower oxide zone compared with the saprolite horizon. These phases have very high Ni and Co contents of up to 19.3 wt% NiO and 5.95 wt% CoO.

EPMA and SEM-EDS data (Figure 11a) reveal a stoichiometric deviation in the direction from serpentine to talc-like clay minerals (kerolite–pimelite end-member) with increasing Ni content. A similar trend has been observed for other Ni laterite deposits in previous studies (Dominican Republic: Villanova-de-Benavent *et al.*, 2014; New Caledonia: Fritsch *et al.*, 2016; Indonesia: Farrokhpay *et al.*, 2019). In contrast, smectite plots in the

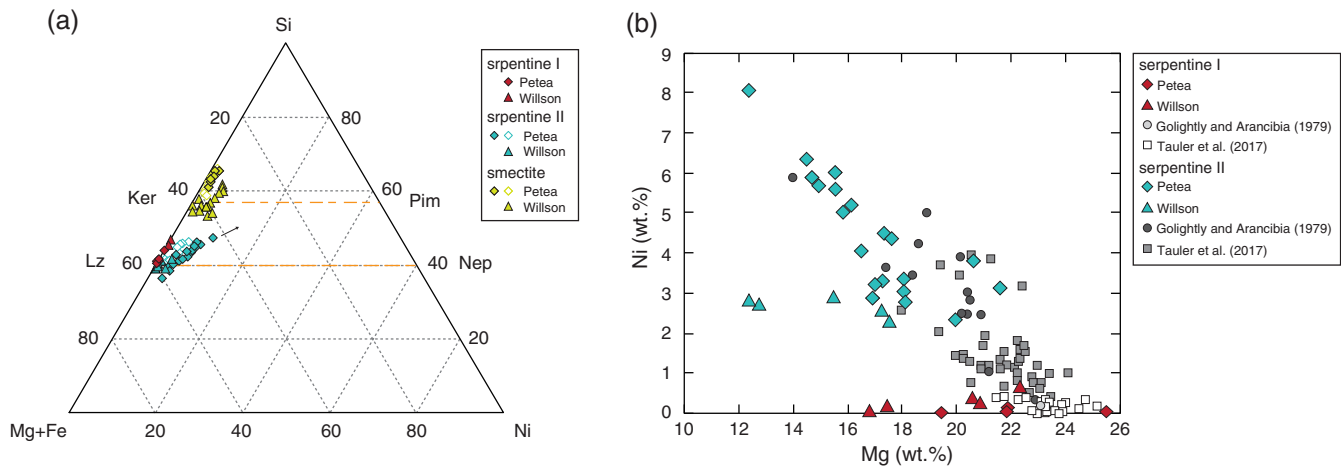


FIGURE 11 (a) Si–(mg + Fe)–Ni ternary diagram for data from serpentine and smectite determined using SEM–EDS and microprobe. Ker, kerolite; Pim, pimelite; Lz, lizardite; Nep, nepouite. (b) Diagram of Ni versus Mg contents in serpentine I and serpentine II in bedrock and saprolite samples from Petea and Willson hills, compared with primary and secondary serpentines from Indonesia of Golightly and Arancibia (1979) and from the Dominican Republic of Tauler *et al.* (2017). Srp-I, serpentine I; Srp-II, serpentine II; Sme, smectite. Symbols show the samples from Petea Hill (20–24, closed diamonds; 20–25 open diamonds) and Willson Hill (22–6, closed triangles). Color coding: Serpentine I (red), serpentine II (bright green), smectite (yellowish green)

area where the proportion of silica is higher than that of serpentine. Ni content in serpentine II is negatively related to Mg content (Figure 11b), which indicates that the enrichment in Ni is attributed to the substitution of Mg in octahedral sites. This trend has been observed in other Ni laterite deposits in both Indonesia and elsewhere (e.g., Golightly and Arancibia, 1979; Tauler *et al.*, 2017; Villanova-de-Benavent *et al.*, 2017).

5 | DISCUSSION

5.1 | Geochemical and mineralogical trends along the profiles

The main chemical components of the studied profiles change from MgO- and SiO₂-rich to Fe₂O₃-rich regolith units toward the surface. The patterns of Mg and Si are essentially similar throughout the profiles, whereby MgO gradually decreases upward from bedrock to saprolite and shows a marked drop in the saprolite–oxide transition zone (i.e., the Mg discontinuity; Freyssinet *et al.*, 2005; Butt and Cluzel, 2013), and SiO₂ content shows a more moderate decrease in the saprolite horizon but with local positive peak values, such as those observed in the lower part of the saprolite horizon of Konde Hill. Fe₂O₃ displays opposite trends to those of MgO and SiO₂, being characterized by a slight increase in the saprolite horizon (from bedrock) and attaining high contents in the saprolite–oxide transition zone (Figures 3 and 4). These geochemical patterns (evolutions) of the studied profiles can be visualized in an AF–M–S ternary

plot (a molar Al–Fe–Mg–Si ternary plot) (Figure 5). The trends of Mg and Si depletion and Fe and Al enrichment from bedrock toward the surface are consistent with the weathering trends in laterite profiles found in previous studies (e.g., Aiglsperger *et al.*, 2016; Putzolu *et al.*, 2019; Ulrich *et al.*, 2019).

The geochemical evolution upward through the profiles can be explained mainly in terms of the breakdown of primary minerals and subsequently by paragenetic evolution within the laterite profiles. Olivine and pyroxene are the minerals that underwent earliest alteration in the laterite profiles of all the studied hills, although more so for Watulabu and Konde hills than Petea and Willson hills. During the early weathering stage, olivine may have been altered to smectite, as supported by petrographic observations of smectite pseudomorphs after olivine in the lower part of the saprolite horizon (Figure 10e). With the progression of weathering, pyroxene has also been replaced by smectite, as shown by SEM–EDS analysis of the middle part of the saprolite horizon (Figure 10f). The low Al contents in olivine pseudomorphs (mean 0.17 wt %) and high Al contents (mean 2.00 wt% Al₂O₃) in pyroxene pseudomorphs also support these processes. Pyroxene alteration into smectite has been reported previously (e.g., Nahon and Colin, 1982; Colin *et al.*, 1990; Tauler *et al.*, 2017; Putzolu *et al.*, 2020), and smectite may also form after olivine (e.g., Nahon *et al.*, 1982; Tauler *et al.*, 2017; Putzolu *et al.*, 2020). Alternatively, olivine and pyroxene may have been directly altered to quartz and goethite without undergoing an intermediate stage, as indicated by XRPD analysis of samples from Watulabu and Konde hills (Figure 8a and Figure 9a,b).

The alteration of serpentine generally starts with the breakdown of olivine and pyroxene (Golightly, 1981). Microscope observations suggest that Ni-poor serpentine I has been progressively replaced by Ni- and Fe-rich serpentine II (Figure 11b). Serpentine II may be formed by ionic exchange of Mg in the octahedral sites of serpentine I by Ni in percolated water (Elias *et al.*, 1981; Golightly, 1981; Freyssinet *et al.*, 2005) or by dissolution–precipitation of serpentine I, accompanied by enrichment in Ni (Villanova-de-Benavent *et al.*, 2016).

With the progression of chemical weathering, under an oxidizing and slightly acidic environment, smectite and serpentine II have been replaced by Fe-(oxy)hydroxides in the oxide zone. This is suggested by the transition from serpentine- and smectite-dominant to goethite-dominant mineral assemblages between the saprolite horizon and the oxide zone (Figure 9a,c,d). In the red laterite sub-horizon, the primary mineral structure has been destroyed, and some goethite has been transformed into hematite (Figure 8a,b), which is a more stable phase near the surface under high-Eh, low-pH conditions (Table 1). The mineralogy of the saprolite–oxide transition zone is characterized by the occurrence of Mn-oxyhydroxides such as lithiophorite, asbolane, and their intermediate phases (Figure 9a,c). Ni–Co-bearing Mn-oxyhydroxides are interpreted to form by secondary precipitation under high-pH and oxidizing conditions (Golightly, 1981; Manceau *et al.*, 1987). The formation of Mn-oxyhydroxides depends strongly on the pH and Eh conditions, which are controlled by fluctuations in the water table, and therefore the distribution of Mn-oxyhydroxides is heterogeneous.

5.2 | Geochemical behavior of nickel and critical metals

5.2.1 | Nickel

The results of whole-rock geochemical analysis show that the distribution and enrichment of Ni are variable with depth and complex compared with other elements. The pattern of enrichment in Ni is strongly influenced by the development of different facies in the laterite profiles, which is controlled mainly by bedrock lithology (the degree of serpentinization). Greater Ni enrichment is observed in the thick saprolite horizons in those profiles that are developed on serpentinized harzburgite (mean 2.06–2.89 wt%) compared with the thin saprolite horizons developed on unserpentinized harzburgite (mean 0.48–1.92 wt%) (Table 1). The mass-balance calculations show that Ni displays moderate to extreme gains in the saprolite horizon relative to bedrock, indicating that supergene

processes played a significant role in the enrichment of Ni in this horizon. The saprolite horizon of Petea Hill shows the highest mean Ni content and an extreme gain in Ni ($\tau_{\text{Ti,Ni}} = +3.94$ to $+22.1$), indicating that additional Ni has been remobilized from a past eroded layer and from nearer the surface than the other studied hills. A similar vertical pattern of Ni content is observed at Willson Hill, although Ni is less enriched in that profile, suggesting that Ni enrichment was associated with the lower degree of weathering of the laterite profile, as indicated by the UMIA (i.e., Petea > Willson).

In contrast, the oxide zone shows low to moderate gains in Ni, with similar mean $\tau_{\text{Ti,Ni}}$ values ranging from $+1.14$ to $+1.84$ in the profiles at Watulabu, Konde, and Willson hills, although Petea Hill shows a greater Ni gain, with a mean $\tau_{\text{Ti,Ni}}$ value of $+4.00$. The mean Ni contents ranging from 1.55 to 1.93 wt% in the oxide zones are fairly uniform relative to those in the saprolite horizons. Considering the mineralogy and SEM–EDS data, goethite is the main Ni-bearing phase in the oxide zones of the studied profiles. The slightly higher mean Ni contents in the oxide zone observed at Petea and Willson hills (1.93 and 2.18 wt%, respectively) compared with the other two hills may indicate that relicts of Ni-bearing silicates are present (Figure 10g), as reported by a previous study (Ulrich *et al.*, 2019).

5.2.2 | Cobalt

Cobalt and Mn display similar behaviors upward through the weathering profiles. The very high mass transfer coefficients for Co and Mn (up to $+32.2$ and $+92.1$, respectively) indicate that these elements have been concentrated by supergene enrichment. Co and Mn are released as Co^{2+} and Mn^{2+} from olivine, the main primary host mineral, and most of these cations have migrated to the lower part of the weathering profile by soil water infiltration owing to their high mobility under slightly acidic conditions ($\sim\text{pH } 5$) in the oxide zone (Table 1). From the saprolite–oxide transition zone to the upper part of the saprolite horizon, pore water pH increases to slightly alkaline conditions ($\text{pH} \approx 7\text{--}8$) by the dissolution of primary silicate minerals, enhancing the oxidation of Mn^{2+} to Mn^{4+} and subsequently their precipitation as Mn-oxyhydroxides in the saprolite–oxide transition zone. Co preferentially enters the structure of low-crystalline Mn-oxyhydroxides by substitution of Mn (Manceau *et al.*, 1987; Roque-Rosell *et al.*, 2010). The formation of Co-bearing Mn-oxyhydroxides may be strongly influenced by physicochemical factors such as drainage conditions, pH, Eh, and O_2 penetration related to the depth from the surface of the profile, as the Mn-oxide

horizon is discontinuous and unevenly distributed in the weathering profiles at Petea and WWillson hills. The fact that the highest contents of Co and Mn are found in the weathering profile at Watulabu Hill suggests that weathering intensity has a lesser influence on the enrichment of these elements. A comparison of the profiles at Watulabu and Willson hills suggests that bedrock mineralogy, particularly olivine content, is of moderate importance in the enrichment of Co and Mn, as it is a source mineral of those elements on account of the higher dissolution rate of olivine relative to serpentine. The highest Co contents observed in the Mn-oxide horizons of Watulabu and Petea hills (1.20 and 0.74 wt% CoO, respectively) are slightly higher than those reported from other Ni laterites in tropical regions (e.g., Roque-Rosell *et al.*, 2010; Aiglsperger *et al.*, 2016; Dublet *et al.*, 2017).

5.2.3 | Scandium

In the studied profiles, Sc shows enrichment, ranging from 24 to 81 ppm in the oxide zone with mean contents of 38–64 ppm, which are similar to or slightly lower than the values reported for other low-grades ore in other countries (e.g., Cuba and Dominican Republic: Aiglsperger *et al.*, 2016; Western Australia: Putzolu *et al.*, 2019; New Caledonia: Ulrich *et al.*, 2019). The vertical profile of Sc shows a residual enrichment pattern that is enhanced in the saprolite–oxide transition zone, as observed for Fe at all of the studied hills (Figures 3 and 4; Figures S1 and S2). This positive relationship between Sc and Fe has been reported in previous studies (Audet, 2008; Aiglsperger *et al.*, 2016; Chasse *et al.*, 2017; Putzolu *et al.*, 2019), indicating that Sc may be enriched in ferric Fe-(oxy)hydroxides (e.g., goethite) by adsorption (Chasse *et al.*, 2017, 2019) or substitution of Fe^{3+} in the crystal structure owing to the similar ionic radius of Sc^{3+} during the alteration of primary silicate minerals (Muñoz *et al.*, 2017; Qin *et al.*, 2020).

Furthermore, the slight negative and positive $\tau_{\text{Ti,Sc}}$ values observed in the red laterite horizon and the upper part of the yellow laterite sub-horizon, respectively (Figures 6 and 7, Figure S4), suggest that some Sc has been released by recrystallization of goethite and transported downward then trapped in relatively newly formed Fe-(oxy)hydroxides. This inferred process is supported by the findings of Ulrich *et al.* (2019), who investigated the relationship between Sc content and transformation of goethite to hematite by Raman spectroscopy for a New Caledonian laterite and showed that progressive dissolution of goethite and subsequent crystallization leads to the release of Sc from iron oxides. Chasse *et al.* (2019) also proposed the remobilization of

Sc and scavenging by goethite through a laterite profile in eastern Australia, based on speciation analysis by X-ray absorption spectroscopy.

The highest Sc content in the oxide zone is roughly consistent with that in bedrock (i.e., Petea > Konde, Willson > Watulabu). This can be explained by differences in the modal abundance of clinopyroxene, as indicated by the positive correlation between Sc and Ca or Al ($R^2 = 0.631$ and $R^2 = 0.897$, respectively), given that clinopyroxene and amphibole, which have high mineral–melt partition coefficients, are the main Sc-bearing minerals in ultramafic rocks (Chasse *et al.*, 2019), and amphibole is uncommon in the studied samples. In this context, the initial Sc content in the bedrock and the later remobilization of Sc by the aging of goethite near the surface and the uptake of Sc into newly formed Fe-(oxy)hydroxides in the upper or middle parts of the oxide zone are important influences on Sc enrichment in the studied profiles.

5.2.4 | Rare-earth elements

REE contents throughout the studied profiles (mean values of 6–48 ppm) for the oxide zone are too low for economic exploitation compared with conventional REE ore deposits (Chakhmouradian and Wall, 2012). However, the high positive $\tau_{\text{Ti,REE}}$ values in the yellow laterite sub-horizon and Mn-oxide horizons (up to $\tau_{\text{Ti,REE}} = +583$) suggest that REEs have been redistributed in the studied profiles during lateritization (Figures 6 and 7). The similar vertical distributions of REEs and Mn observed in all profiles suggest that the geochemical behavior of Mn is an important control on REE mobilization. REEs released by the dissolution of primary silicates, mostly pyroxenes, may have been adsorbed onto poorly crystallized Fe- and Mn-(oxy)hydroxides during early weathering. The progression of weathering enhances dissolution and recrystallization of goethite, leading to the release of REEs from goethite near the surface of the laterite profile and accumulation by adsorption onto Mn-oxyhydroxides in the saprolite–laterite transition zone (e.g., Aiglsperger *et al.*, 2016; Ulrich *et al.*, 2019). This process may have contributed to different degrees of REE enrichment, consistent with the lower REE contents of the more weathered profiles (i.e., Konde and Petea hills) relative to the less weathered profiles (i.e., Watulabu and Willson hills) (Table 1).

The REE patterns, normalized to C1 chondrite (Anders and Grevesse, 1989) show that light REEs (LREEs: La to Eu) become preferentially enriched over heavy REEs (HREEs: Gd to Lu) toward the surface (Figure S5). Given the same valence (except for Ce) and decreasing ion radius from LREEs to HREEs, it is

expected that the adsorption of REEs onto Fe- or Mn-(oxy)hydroxides is more pronounced for HREEs than LREEs. However, HREEs form more stable dissolved complexes compared with LREEs when dissolved inorganic carbon is abundant in solution, inhibiting the surface complexation of HREEs onto metal (oxy)hydroxides and leaving them in solution (e.g., Erel and Stolper, 1993; Byrne and Sholkovitz, 1996). In the studied profiles, aging of Fe- and Mn-(oxy)hydroxides may release REEs to soil water. HREEs then form complexes with bicarbonate ions and being removed from the profiles on account of their high mobility, whereas LREEs are scavenged by later-formed Mn-oxyhydroxides in deeper parts of the profiles. Regarding Ce, this element may be oxidized from Ce^{3+} to Ce^{4+} by Mn-oxyhydroxides (Ohta and Kawabe, 2001) and is subsequently precipitated as an insoluble phase, such as Ce^{4+} oxide and/or phosphate (e.g., Aiglsperger *et al.*, 2016). The gradual dissolution of Mn-oxyhydroxides with the progression of weathering may leach all trivalent REEs, leaving Ce in the upper part of the profile. This may have resulted in the formation of the red laterite sub-horizon with a positive Ce anomaly and lower REE contents, and the yellow laterite sub-horizon or Mn-oxide horizon with a negative Ce anomaly and higher REE contents (Figure S5). These trends have been described in previous studies (Aiglsperger *et al.*, 2016; Ulrich *et al.*, 2019).

5.2.5 | Palladium and platinum

Pt and Pd show a residual-type enrichment pattern, with mean contents of 36–66 ppb in the oxide zones of studied profiles (Figures 3 and 4). These values are similar to or slightly lower than those reported from Ni laterites worldwide, which are up to several hundred ppb as total PGE contents, but mostly <100 ppb (e.g., Eliopoulos and Economou-Eliopoulos, 2000; Traore *et al.*, 2008b; Aiglsperger *et al.*, 2015, 2016), although some laterite deposits in western Australia have been reported to contain a few ppm of PGEs (Gray *et al.*, 1996). The residual enrichment of Pt + Pd is supported by previous reports of PGE enrichment in laterite profiles as accessory PGE minerals protected within resistant Cr-spinel (Traore *et al.*, 2008b; Aiglsperger *et al.*, 2015). However, the mass transfer coefficients of Pt + Pd ($\tau_{Ti,Pt+Pd}$) typically show negative values throughout the weathering profiles, except for Petea Hill and a few samples from Konde and Willson hills (Table 1). Thus, most Pt and Pd may have been removed from these profiles and the remainder concentrated near the surface by residual enrichment during lateritization, although it should be noted that Pt + Pd contents of the unweathered ultramafic rocks are highly heterogeneous (Table 1).

Positive $\tau_{Ti,Pt+Pd}$ values observed from the upper part of the saprolite horizon to near the surface at Petea Hill (up to +8.17) indicate that Pt and Pd have been redistributed and enriched by supergene processes in this profile (Figure 7). These elements may have been leached into pore water by the dissolution of PGE minerals existing in bedrock as alloy and sulfide phases under conditions of high Eh and low-moderate pH near the surface. Dissolved Pt and Pd ions in pore water may have been mobilized and precipitated as neo-formed minerals by bioreduction and/or incorporated into Fe- or Mn-oxyhydroxides close to the surface, as proposed by previous studies (Gray *et al.*, 1996; Cabral *et al.*, 2011; Aiglsperger *et al.*, 2015). The high positive $\tau_{Ti,Pt+Pd}$ value observed in the Mn-oxide horizon at Petea Hill supports this explanation.

Moreover, the distribution patterns of Pt and Pd are decoupled in the upper part of the oxide zone, with Pd content being lower than that of Pt in the studied profiles (apart from Petea Hill, where these elements show similar patterns) (Table 1). Considering the higher oxidation potential of Pt to enter solution, it is expected that Pt is less soluble and less mobile than Pd in near-surface environments (Sassani and Shock, 1998; Colombo *et al.*, 2008; Reith *et al.*, 2014). Once dissolved, Pd is likely leached out from the weathering profiles, as indicated by the fact that greater Pd enrichment relative to Pt was not observed through the studied profiles. The decoupling of the distributions of Pt and Pd may reflect the redox environment that differentially controls their behaviors in the near-surface region of the profiles.

The enrichment of Pt and Pd in the studied profiles can be explained mainly by residual concentration as impurities in weathering-resistant minerals, such as Cr-spinel, and subsequent remobilization then reduction and precipitation controlled by the presence of Fe- and Mn-oxyhydroxides and/or bioactivity. Despite the similar range of Pt and Pd contents in bedrock, these elements are less enriched in the studied profiles than in other Ni laterites (up to several hundred ppb) in the Caribbean and Brazil (Aiglsperger *et al.*, 2016; Rivera *et al.*, 2018). This may be attributed to the environmental setting of the study area, with the heavy rainfall of Sulawesi contributing to deep oxidative weathering, resulting in lesser enrichment of Pt and Pd.

5.3 | Ni remobilization processes indicated by the correlation between gained Ni and Fe amounts

The calculation results for amounts of Ni lost and gained show large positive values for all studied hills, meaning

that Ni has been mobilized and added from past eroded layers to the present weathering profiles (Table S1). Among the elements for which the mass-balance calculation shows gains, the amounts of gained Ni show a stronger positive correlation with those of Fe ($R^2 = 0.75$) compared with other major and minor elements ($R^2 = 0.45, 0.27, 0.33$, and 0.27 for Al, Cr, Mn, and Co, respectively), suggesting that the geochemical behavior of Fe influences Ni mobilization during chemical weathering. As the profiles of Konde and Petea hills show greater amounts of gained Ni and Fe than those of Watulabu and Willson hills, it is inferred that these elements tend to be more mobilized in the more highly weathered profiles in the case of similar bedrock (i.e., fresh harzburgite or serpentinized harzburgite) (Figure 12, Table S1). The calculation results for other Ni laterite deposits in tropical to subtropical regions such as the Caribbean (Cuba and the Dominican Republic), Myanmar, and Indonesia also show a positive relationship between the amounts of gained Fe and Ni, suggesting that Fe remobilization may contribute to Ni enrichment in other tropical to subtropical regions (Figure 12). However, results for these other deposits show a lower ratio of gained Fe to Ni (Fe/Ni) compared with the studied Indonesian Ni laterite deposits. This is likely due to differences in the Ni-bearing phases. Ni laterite profiles from the Dominican Republic (Loma Caribe and Loma Peguera), which show lower Fe/Ni (Figure 12), contain garnierite minerals (e.g., kerolite and

sepiolite) in the saprolite horizon (Villanova-de-Benavent *et al.*, 2014). These minerals concentrate more Ni than serpentine II, and we therefore infer that Fe/Ni becomes low when the weathering profile includes the formation or presence of garnierite.

Petea Hill shows the highest gained amounts of both Ni and Fe compared with the other studied Indonesian profiles and Ni laterite deposits developed in other tropical to subtropical regions (Figure 12). As suggested by the presence of abundant Fe^{3+} -(oxy)hydroxides (such as goethite and hematite) in oxide zones measuring several meters thick, the studied laterite profiles are expected to have undergone more intense oxidative weathering, which may have restricted Fe remobilization owing to the complete oxidation of Fe^{2+} under high levels of O_2 . Despite such a condition, the fact that Petea Hill shows a significant gain of Fe suggests that this element may have been remobilized by the dissolution of Fe^{3+} -(oxy)hydroxides. Dublet *et al.* (2015) reported that aging of goethite enhances crystallinity and transformation to hematite, resulting in depletion of Ni in the upper part of the oxide zone. Although the factors influencing the dissolution of Fe^{3+} -(oxy)hydroxides remain unclear, the accumulated organic matter in the near-surface horizon is likely to produce a reducing environment and enhance microbial reduction and/or organic-ligand-promoted dissolution of Fe^{3+} -(oxy)hydroxides because Fe^{3+} -(oxy)hydroxides are unlikely to dissolve under the slightly acidic ($\text{pH} = \sim 5\text{--}6$) and oxic environment of an oxide zone.

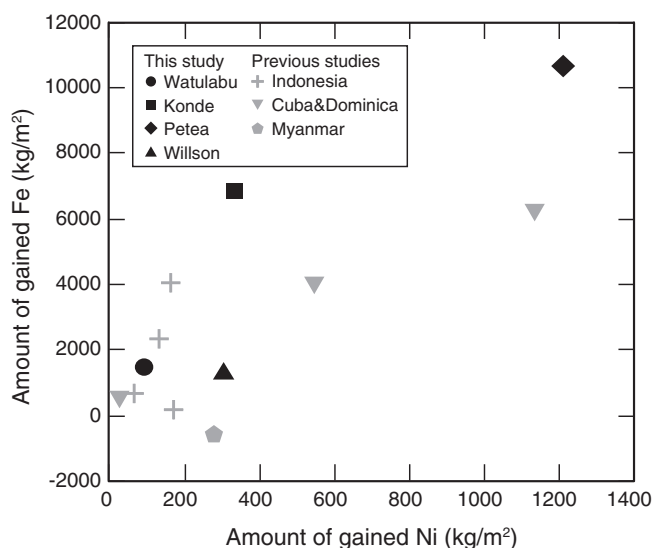


FIGURE 12 Diagram of the amounts of gained Ni and Fe (kg/m^2) through the present laterite profiles with data from the studied hills in the Soroako and Pomalaa mining areas. Also shown are data for laterite profiles from previous studies (Myanmar, Schellmann, 1989; Indonesia, Sufriadin *et al.*, 2011; Cuba and the Dominican Republic, Aiglsperger *et al.*, 2016)

5.4 | Influence of fixation on Ni enrichment as inferred from the variation in Ni-bearing minerals in the saprolite horizon

As discussed above, Ni enrichment in the present profiles could be associated with Ni gained from eroded former layers and the uppermost parts of profiles. Among the studied profiles, higher Ni gains are observed in the saprolite horizon than in the oxide zone at Petea and Willson hills (Table S1), suggesting that more mobilized Ni has been transported downward in solution and accumulated in the profiles of these hills than at Konde and Watulabu. Therefore, the mobilization of Ni is one of the most important factors for its enrichment in the laterite deposits. However, the fixation process (i.e., the formation of high-Ni-content minerals) may also contribute to the large Ni gain in the laterite profiles during chemical weathering of ultramafic bedrock.

As shown by XRPD, SEM-EDS, and microscope analyses, the main Ni-bearing mineral in the saprolite horizon at Petea and Willson hills is Ni- and Fe-rich,

Mg-poor serpentine II, which has been reported from other Ni laterite deposits (e.g., Golightly and Arancibia, 1979; Sufriadin *et al.*, 2011; Fu *et al.*, 2014; Villanova-de-Benavent *et al.*, 2017). Serpentine II is commonly observed at thin-section scale along the mesh-like textures of serpentine I, and it may therefore result from the replacement of serpentine I accompanied by enrichment in Ni. Furthermore, the contents of Mg and Ni, which are octahedral elements, in serpentine II are negatively correlated (Figure 11b) in saprolite samples from both Petea and Willson hills, indicating that Mg is substituted by Ni. Although Fe and Mg also show a negative correlation (Figure S6a), the slope of the trend is gentle when compared with that for Ni and Mg, suggesting that Ni content increases more markedly than Fe during weathering, similar to the results previously reported for tropical region Ni laterite deposits (Golightly and Arancibia, 1979; Tauler *et al.*, 2017; Villanova-de-Benavent *et al.*, 2017). The negative correlation is more clearly defined between Ni + Fe and Mg (Figure S6b), suggesting that both Ni and Fe become present by substitution of Mg in octahedral sites. These trends can be seen in the saprolite samples from both Petea and Willson hills, implying that the Ni enrichment process in these two profiles is essentially the same. Moreover, serpentine II in the saprolite samples from Petea Hill is characterized by lower Mg and higher Ni and Fe contents compared with Willson Hill (Figure S6b), indicating that Mg substitution in octahedral sites has progressed further at Petea Hill. This pattern of Ni content in serpentine II corresponds to the difference between Petea and Willson hills in the gained Ni in the weathering profiles. Therefore, Ni mobilization is the key process controlling Ni enrichment in the saprolite horizon, rather than the fixation process, particularly in the laterite profiles developed on serpentinized harzburgite (Petea and Willson hills).

Although smectite is observed in saprolite samples from Petea and Willson hills as an Ni-bearing secondary phase, XRPD data and comprehensive SEM-EDS analysis at thin-section scale show that this mineral has a less common occurrence in the middle to upper parts of the saprolite horizon where Ni shows highest levels of enrichment in the profiles at these two hills (Figure 8b and 9c,d). This may be because smectite is unstable under oxidative weathering conditions, and in turn, is easily replaced by Fe-(oxy)hydroxides and quartz during weathering (Fu *et al.*, 2014) (Figure 10c,f). Previous studies have also shown that smectite is rare in saprolite samples from Soroako and other Ni laterite deposits in Indonesia (Sufriadin *et al.*, 2011; Fu *et al.*, 2014; Farrokhpay *et al.*, 2019). Therefore, smectite is likely a less important phase for Ni enrichment compared with

serpentine II in the saprolite horizons at both the Petea and Willson hill profiles.

Konde and Watulabu hills, where the bedrock is composed of unserpentinized harzburgite, show higher gained amounts of Ni in the oxide zone. Weathering profiles at these hills have thick oxide zones and thin saprolite horizons compared with those at Petea and Willson hills. These differences can be explained by the higher dissolution rate of olivine, the abundant primary mineral in fresh harzburgite, relative to serpentine, which is the main mineral of serpentinized harzburgite. Because Ni-bearing clays such as serpentine and smectite are absent in the saprolite horizon formed above fresh peridotite, most Mg, Si, and Ni released from primary silicate minerals is leached from weathering profiles and partly precipitated as greenish garnierite in the bedrock within the lowermost part of the saprolite horizon. Moreover, excess dissolved Si forms quartz, generally leading to dilution of Ni content in the saprolite horizon (Golightly, 1981). These geochemical characteristics are observed in the weathering profile at Konde Hill, which is the most highly weathered of the studied profiles. Although the saprolite samples from Watulabu Hill contain Ni-bearing serpentine that may have been formed by replacement of primary olivine or pyroxene, this serpentine is altered to quartz and goethite with the progression of chemical weathering (Figure 9a). Therefore, in the cases of Watulabu and Konde hills, whose profiles are developed on unserpentinized peridotite, the Ni fixation process does not play a major role in Ni enrichment of the saprolite horizon.

5.5 | Key processes controlling strong Ni enrichment

As discussed in Sections 5.3 and 5.4, Ni remobilization from the surface downward to the saprolite horizon where Ni is fixed mainly as Ni-bearing serpentine by substitution of Mg in octahedral sites is important for significant Ni enrichment, especially in the laterite profiles developed on serpentinized peridotite. Moreover, the positive correlation between the amounts of gained Fe and Ni in the present profiles (Figure 12) indicates that the behavior of Fe may influence Ni mobilization processes during the chemical weathering of ultramafic rocks. This correlation suggests that Fe remobilization that occurred in previously eroded layers and the near-surface horizon may be important for the marked Ni enrichment in the saprolite horizon. On the basis of these geochemical and mineralogical data, we propose possible Ni enrichment processes for the laterite profile of Petea Hill, as follows (Figure 13).

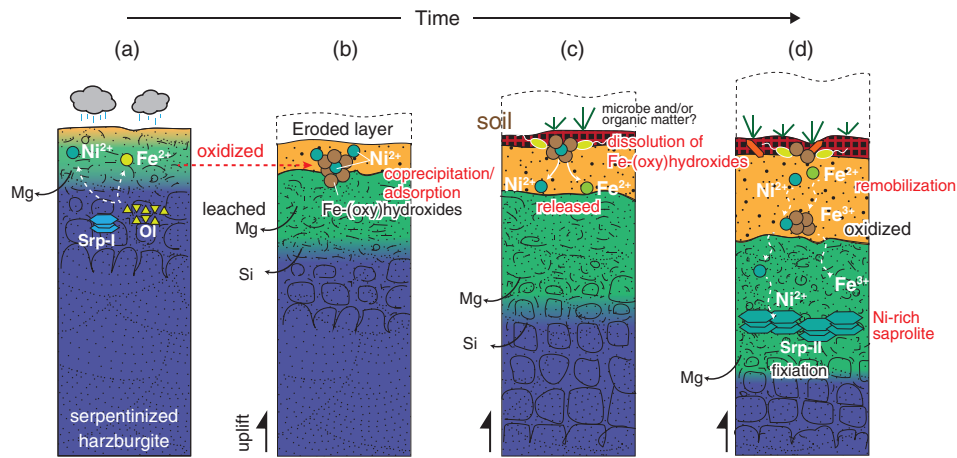


FIGURE 13 Evolution of Petea Hill and proposed Ni enrichment processes in the saprolite horizon. (a) Ni and Fe are released by dissolution of primary olivine (and serpentine I), then Ni is incorporated into Fe-(oxy)hydroxides formed under an oxidizing environment in the near-surface part of the profile during the early stage of weathering. (b) Progressive weathering leads to the leaching of Mg and Si, with Ni content reaching up to ~1 wt% as residual enrichment. (c) after the formation of surficial soil, accumulated organic matter and/or microbial activity produce a low-pH or reducing environment, resulting in dissolution of Fe-(oxy)hydroxides and release of Fe and Ni into the soil solution. (d) Dissolved Fe and Ni are transported downward, then Fe is precipitated mainly in the oxide zone as Fe-(oxy)hydroxides, whereas most of the remobilized Ni passes through the oxide zone into the saprolite horizon and is fixed in Ni-bearing serpentine II by substitution of Mg in octahedral sites. Ol, olivine; Srp-I, serpentine I; Srp-II, serpentine II

During the early stage of weathering, primary silicate minerals in the bedrock are altered to Fe^{3+} -(oxy)hydroxides as a result of hydrolysis and oxidation processes at the surface (Figure 13a). With the progression of chemical weathering, the surface horizon shows marked decreases in Mg and Si, and increases in Fe and Ni as residual phases. Ni^{2+} released from primary minerals such as olivine and serpentine I is incorporated into goethite by substitution of Fe^{3+} in the crystal structure and adsorption onto its surface (Figure 13b). Ni content in the oxide zone increases via this residual enrichment process (Freyssinet *et al.*, 2005). Continuing intensive weathering and regional uplift lead to movement of the weathering front downward and to the development of a saprolite horizon (Golightly, 1981; Freyssinet *et al.*, 2005; Butt and Cluzel, 2013) (Figure 13b). Most of the serpentine I is altered to serpentine II, which contains Fe and Ni by substitution of Mg in its octahedral sites, as indicated by the preserved original mesh texture. Simultaneously, soil is formed, and organic matter accumulates at the surface of the profile (Figure 13c).

The surficial soil may produce a reducing environment, especially during the rainy season because of the elevated water table, leading to the dissolution of Ni-bearing goethite and leaching Ni and Fe into the soil solution (Figure 13c). Although dissolved Ni is partly taken up by newly formed Fe^{3+} -(oxy)hydroxides in the oxide zone, the remainder is transported downward and fixed by substitution of Mg in the octahedral sites of serpentine II in the saprolite horizon (Figure 13d). This process can promote supergene enrichment of Ni in the

laterite profile at Petea Hill. Previous studies have shown that in the oxide zone, Ni is incorporated into the structure of Fe^{3+} -(oxy)hydroxides rather than adsorbed onto their surfaces (e.g., Dublet *et al.*, 2012; Fan and Gerson, 2015). In general, incorporated Ni is much less easily released into solution compared with adsorbed Ni. Therefore, the dissolution of Fe^{3+} -(oxy)hydroxides by microbial reduction and/or organic-ligand-promoted dissolution in surficial soil is likely to be an important process for pronounced Ni enrichment in the saprolite horizon. As this process is expected to proceed more rapidly than surface erosion in a well-developed profile that has surficial soil, the gained amount of Ni becomes greater than that of Fe, as seen at Petea Hill (Figure 12).

This model of Ni enrichment should be applicable to many Ni laterite deposits developed under tropical to subtropical climatic conditions, although it is not possible to directly compare the gained Fe and Ni between profiles with different Ni-bearing minerals. The finding of this study that large gained amounts of Fe may indicate large gains of Ni in the profile is important in understanding the factors controlling Ni enrichment at both regional and deposit scales.

6 | CONCLUSIONS

The present study investigated the geochemical and mineralogical evolution of laterite profiles developed on

different bedrock lithologies. The combination of geochemical and mineralogical analyses, together with mass-balance calculations, provides a better understanding of enrichment in critical metals and the relevant processes, and constrains the geochemical factors controlling downward Ni remobilization and enrichment in the saprolite horizon. The main conclusions of the study are as follows.

- Cobalt and REEs show pronounced gains in the studied profiles and strong correlations with Mn enrichment, with the highest contents being observed in the saprolite–oxide transition zone. Thus, the supergene processes of these elements may be controlled by the behavior of Mn, involving remobilization and reprecipitation under variable pH and Eh conditions. The formation of Mn-oxyhydroxides is strongly influenced by physicochemical conditions, although the greatest enrichment of Co and REEs, which is observed in the Mn-oxide horizon at Watulabu Hill, suggests that bedrock dominated by olivine may also contribute to this enrichment. Contents of Co of the studied laterite profiles are sufficiently high for it to be considered as a potential by-product element, although the highly heterogeneous spatial distribution of Co-bearing Mn-oxide horizons would make exploration difficult.
- Scandium, Pt, and Pd show similar patterns of contents and τ values in the studied profiles to those of Fe and Al, suggesting that these elements are residually enriched rather than a result of supergene processes and that the enrichments are controlled mainly by initial elemental contents in bedrock. The mean Sc content of 55 ppm is similar to or slightly lower than those of other Ni laterite deposits. Sc is released by pyroxene dissolution and incorporated into goethite. The intensive weathering may mobilize Sc as a result of dissolution and recrystallization of goethite in the top of the profile, leading to remobilization downward and accumulation in the yellow laterite sub-horizon. Platinum and Pd are likely to be enriched as impurities in residual Cr-spinel, although most of these elements may have been removed from the studied laterite profiles under tropical weathering with heavy rainfall and oxidative conditions in Indonesia, as indicated by negative τ values.
- Nickel enrichment is linked to the development of saprolite horizons, which is controlled primarily by the degree of serpentinization of bedrock. The greatest enrichment was observed in the saprolite horizon of Petea Hill, where bedrock is serpentinized harzburgite and the profile is highly weathered.

Mineralogical observations revealed that the main Ni-bearing mineral of the saprolite horizon in the studied profiles is Ni-rich serpentine, and Ni and Fe are enriched in these minerals by substitution for Mg in octahedral sites. Mass-balance calculations show that the amounts of gained Ni and Fe are positively correlated, suggesting that the behavior of Fe may affect Ni mobilization processes during chemical weathering. Combining these findings, it is inferred that Ni enrichment in the saprolite horizon may reflect the amount of remobilized Ni derived from the upper horizons and from past eroded layers, and may also be controlled by the geochemical behavior of Fe rather than the variation in abundance of Ni-bearing minerals. Therefore, a large gained amount of Fe can be an indicator of strong Ni enrichment in the saprolite horizon, at both regional and deposit scales. The substantial gains of both Ni and Fe at Petea Hill are greater than those of other Ni laterites in tropical and subtropical regions. The dissolution of Ni-bearing goethite by processes involving microbial reduction and/or organic-ligand-promoted dissolution at or near the surface leads to the downward remobilization of Ni and significant Ni enrichment in the saprolite horizon. These geochemical processes may be enhanced under humid and hot climatic conditions such as those prevailing in Indonesia.

ACKNOWLEDGMENTS

The authors are grateful to S. Suyuti (PT Vale, Soroako), A. Malamu (PT Vale, Pomalaa), and geologists of PT Vale Indonesia in the Soroako and Pomalaa mines for their help and hospitality during fieldwork. We thank A. Matsumoto, Y. Ohtomo, T. Ikeshima, and A. Murofushi for their technical assistance during XRF and EPMA data acquisition. We also express our gratitude to Dr. Hayashi for editorial handling and to two anonymous reviewers for their constructive comments on an earlier version of the manuscript. This research was supported by a student overseas field survey grant of the Japan Mining Industry Association, a Joint Research Grant of the “Nanotechnology Platform” Program of the Ministry of Education, Culture, Sports, Science, and Technology (MEXT), the Japan Society for the Promotion of Science (JSPS) KAKENHI 17H03502 to T. Otake, and the Japan Society for the Promotion of Science (JSPS) KAKENHI 19K24388 and a Grant-in-Aid for JSPS Fellows 18J11243 to A. Ito.

DATA AVAILABILITY STATEMENT

The data that support the findings of this study are available from the corresponding author upon reasonable request.

ORCID

Akane Ito  <https://orcid.org/0000-0001-6406-3156>
 Tsubasa Otake  <https://orcid.org/0000-0001-9596-4141>
 Adi Maulana  <https://orcid.org/0000-0001-9349-0106>
 Kenzo Sanematsu  <https://orcid.org/0000-0002-9102-8265>
 Sufriadin  <https://orcid.org/0000-0002-6103-3143>
 Tsutomu Sato  <https://orcid.org/0000-0002-3279-3696>

REFERENCES

- Aiglsperger, T., Proenza, J.A., Lewis, J.F., Labrador, M., Svojtka, M., Rojas-Puron, A., Longo, F. and Durisova, J. (2016) Critical metals (REE, Sc, PGE) in Ni laterites from Cuba and The Dominican Republic. *Ore Geology Reviews*, 73, 127–147.
- Aiglsperger, T., Proenza, J.A., Zaccarini, F., Lewis, J.F., Garuti, G., Labrador, M. and Longo, F. (2015) Platinum group minerals (PGM) in the Falcondo Ni-laterite deposit, Loma Caribe peridotite (Dominican Republic). *Mineralium Deposita*, 50, 105–123.
- Anders, E. and Grevesse, N. (1989) Abundances of the elements: meteoritic and solar. *Geochimica et Cosmochimica Acta*, 53, 197–214.
- Audet, M.A. (2008) *Le massif du Koniambo-Nouvelle Calédonie: Formation et obduction d'un complexe ophiolitique de type SSZ. Enrichissement en nickel, cobalt et scandium dans les profils résiduels*. PhD thesis (in French), Université de Nouvelle Calédonie, p. 327.
- Babechuk, M.G., Widdowson, M. and Kamber, B.S. (2014) Quantifying chemical weathering intensity and trace element release from two contrasting basalt profiles, Deccan traps, India. *Chemical Geology*, 363, 56–75.
- Brimhall, G.H. and Dietrich, W.E. (1987) Constitutive mass balance relations between chemical composition, volume, density, porosity, and strain in metasomatic hydrochemical systems: results on weathering and pedogenesis. *Geochimica et Cosmochimica Acta*, 51, 567–587.
- Butt, C.R.M. and Cluzel, D. (2013) Nickel laterite ore deposits: weathered Serpentinities. *Elements*, 9, 123–128.
- Byrne, R.H. and Sholkovitz, E.R. (1996) Chapter 158 marine chemistry and geochemistry of the lanthanides. In: *Handbook on the Physics and Chemistry of Rare Earths*, Vol. 23. Amsterdam: Elsevier, pp. 497–593.
- Cabral, A.R., Radtke, M., Munnik, F., Lehmann, B., Reinholz, U., Riesemeier, H., Tupinamba, M. and Kwitko-Ribeiro, R. (2011) Iodine in alluvial platinum-palladium nuggets: evidence for biogenic precious-metal fixation. *Chemical Geology*, 281, 125–132.
- Chadwick, O.A., Brimhall, G.H. and Hendricks, D.M. (1990) From black box to a grey box: a mass balance interpretation of pedogenesis. *Geomorphology*, 3, 369–390.
- Chakhmouradian, A.R. and Wall, F. (2012) Rare earth elements: minerals, mines, magnets. *Elements*, 8, 333–340.
- Chasse, M., Griffin, W.L., O'Reilly, S.Y. and Calas, G. (2017) Scandium speciation in a world-class lateritic deposit. *Geochemical Perspectives Letters*, 3, 105–113.
- Chasse, M., Griffin, W.L., O'Reilly, S.Y. and Calas, G. (2019) Australian laterites reveal mechanisms governing scandium dynamics in the critical zone. *Geochimica et Cosmochimica Acta*, 260, 292–310.
- Cluzel, D. and Vigier, B. (2008) Syntectonic mobility of supergene nickel ores of New Caledonia (Southwest Pacific). Evidence from garnierite veins and faulted regolith. *Resource Geology*, 58, 161–170.
- Colin, F., Nahon, D., Trescases, J.J. and Melfi, A.J. (1990) Lateritic weathering of pyroxenites at Niquelandia, Goias, Brazil: the supergene behavior of nickel. *Economic Geology*, 85, 1010–1023.
- Colombo, C., Oates, C.J., Monhemius, A.J. and Plant, J.A. (2008) Complexation of platinum, palladium and rhodium with inorganic ligands in the environment. *Geochemistry-Exploration Environment Analysis*, 8, 91–101.
- Dublet, G., Juillot, F., Brest, J., Noel, V., Fritsch, E., Proux, O., Olivi, L., Ploquin, F. and Morin, G. (2017) Vertical changes of the co and Mn speciation along a lateritic regolith developed on peridotites (New Caledonia). *Geochimica et Cosmochimica Acta*, 217, 1–15.
- Dublet, G., Juillot, F., Morin, G., Fritsch, E., Fandeur, D. and Brown, G.E. (2015) Goethite aging explains Ni depletion in upper units of ultramafic lateritic ores from New Caledonia. *Geochimica et Cosmochimica Acta*, 160, 1–15.
- Dublet, G., Juillot, F., Morin, G., Fritsch, E., Fandeur, D., Ona-Nguema, G. and Brown, G.E. (2012) Ni speciation in a new Caledonian lateritic regolith: a quantitative X-ray absorption spectroscopy investigation. *Geochimica et Cosmochimica Acta*, 95, 119–133.
- Dzemua, G.L., Gleeson, S.A. and Schofield, P.F. (2013) Mineralogical characterization of the Nkamouna co-Mn laterite ore, Southeast Cameroon. *Mineralium Deposita*, 48, 155–171.
- Elias, M., Donaldson, M.J. and Giorgetta, N. (1981) Geology, mineralogy, and chemistry of lateritic nickel-cobalt deposits near Kalgoorlie, Western Australia. *Economic Geology*, 76, 1775–1783.
- Eliopoulos, D.G. and Economou-Eliopoulos, M. (2000) Geochemical and mineralogical characteristics of Fe-Ni- and bauxitic-laterite deposits of Greece. *Ore Geology Reviews*, 16, 41–58.
- Erel, Y. and Stolper, E.M. (1993) Modeling of rare-earth element partitioning between particles and solution in aquatic environments. *Geochimica et Cosmochimica Acta*, 57, 513–518.
- Fan, R. and Gerson, A.R. (2015) Synchrotron micro-spectroscopic examination of Indonesian nickel laterites. *American Mineralogist*, 100, 926–934.
- Farrokhpay, S., Cathelineau, M., Blancher, S.B., Laugier, O. and Filippov, L. (2019) Characterization of Weda bay nickel laterite ore from Indonesia. *Journal of Geochemical Exploration*, 196, 270–281.
- Freyssinet, P., Butt, C.R.M., Morris, R.C. and Piantone, P. (2005) Ore-forming processes related to lateritic weathering. *Economic Geology*, 100, 681–722.
- Fritsch, E., Juillot, F., Dublet, G., Fonteneau, L., Fandeur, D., Martin, E., Caner, L., Auzende, A.L., Grauby, O. and Beaufort, D. (2016) An alternative model for the formation of hydrous mg/Ni layer silicates ('deweylite'/garnierite) in faulted peridotites of New Caledonia: I. Texture and mineralogy of a paragenetic succession of silicate infillings. *European Journal of Mineralogy*, 28, 295–311.
- Fu, W., Yang, J.W., Yang, M.L., Pang, B.C., Liu, X.J., Niu, H.J. and Huang, X.R. (2014) Mineralogical and geochemical characteristics of a serpentinite-derived laterite profile from East Sulawesi, Indonesia: implications for the lateritization process and Ni

- supergene enrichment in the tropical rainforest. *Journal of Asian Earth Sciences*, 93, 74–88.
- Gleeson, S.A., Butt, C.R.M. and Elias, M. (2003) Nickel laterites: a review. *SEG Newsletter, Society of Economic Geology*, 54, 9–16.
- Golightly, J.P. (1979) *Geology of Soroako Nickeliferous Laterite Deposit*. Ontario, Canada: INCO Metals Company.
- Golightly, J.P. (1981) Nickeliferous laterite deposits. *Economic Geology*, 75, 710–735.
- Golightly, J.P. (2010) Progress in understanding the evolution of nickel laterites. *Society of Economic Geologists Special Publication*, 15, 451–475.
- Golightly, J.P. and Arancibia, O.N. (1979) The chemical composition and infrared spectrum of nickel- and iron- substituted serpentine from a nickeliferous laterite profile, Soroako, Indonesia. *Canadian Mineralogist*, 17, 719–728.
- Gray, D.J., Schorin, K.H. and Butt, C.R.M. (1996) Mineral associations of platinum and palladium in lateritic regolith, Ora Banda sill, Western Australia. *Journal of Geochemical Exploration*, 57, 245–255.
- Hall, R. and Wilson, M.E.J. (2000) Neogene sutures in eastern Indonesia. *Journal of Asian Earth Sciences*, 18, 781–808.
- Hoffman, E.L. and Dunn, B. (2002) Sample preparation and bulk analytical methods for PGE. In: Cabri, L.J. (Ed.), *The Geology, Geochemistry and Mineral Beneficiation of Platinum Group Elements*, Vol. 54. Montreal: Canadian Institute of Mining, Metallurgy and Petroleum. pp. 1–11.
- Ilyas, A., Kashiwaya, K. and Koike, K. (2016) Ni grade distribution in laterite characterized from geostatistics, topography and the paleo-groundwater system in Sorowako, Indonesia. *Journal of Geochemical Exploration*, 165, 174–188.
- Ilyas, A. and Koike, K. (2012) Geostatistical modeling of ore grade distribution from geomorphic characterization in a laterite nickel deposit. *Natural Resources Research*, 21, 177–191.
- Kadarusman, A., Miyashita, S., Maruyama, S., Parkinson, C.D. and Ishikawa, A. (2004) Petrology, geochemistry and paleogeographic reconstruction of the East Sulawesi Ophiolite, Indonesia. *Tectonophysics*, 392, 55–83.
- MacPherson, C.G. and Hall, R. (2002) Timing and tectonic controls in the evolving orogen of SE Asia and the western Pacific and some implications for ore generation. *Timing and Location of Major Ore Deposits in an Evolving Orogen*, 204, 49–67.
- Manceau, A., Llorca, S. and Calas, G. (1987) Crystal chemistry of cobalt and nickel in lithiophorite and asbolane from New Caledonia. *Geochimica et Cosmochimica Acta*, 51, 105–113.
- Maulana, A., Christy, A.G., Ellis, D.J., Imai, A. and Watanabe, K. (2013) Geochemistry of eclogite- and blueschist-facies rocks from the Bantimala complex, South Sulawesi, Indonesia: Protolith origin and tectonic setting. *Island Arc*, 22, 427–452.
- Maulana, A., Sanematsu, K. and Sakakibara, M. (2016) An overview on the possibility of scandium and REE occurrence in Sulawesi, Indonesia. *Indonesian Journal of Geoscience*, 3, 139–147.
- Maurizot, P., Sevin, B., Iseppi, M. and Giband, T. (2019) Nickel-bearing laterite deposits in accretionary context and the case of New Caledonia: from the large-scale structure of earth to our everyday appliances. *Geological Society of America Today*, 29(5), 4–10.
- McRae, M.E. (2020) Nickel. *USGS Mineral Commodity Summaries*, 112–113.
- Mubroto, B., Briden, J.C., McClelland, E. and Hall, R. (1994) Paleomagnetism of the Balantak ophiolite, Sulawesi. *Earth and Planetary Science Letters*, 125, 193–209.
- Muñoz, M., Ulrich, M., Levard, C., Rose, J., Ambrosi, J.P., Cathelineau, M., Teitler, Y., Marcaillou, C. and Hesse, B. (2017) *Distribution and Speciation of Sc in Lateritic Profiles of New Caledonia Using Synchrotron-XRF and Sc K-Edge XANES Spectroscopy*. Nancy: First International Workshop on the Geochemical Cycle of Nickel.
- Nahon, D., Colin, F. and Tardy, Y. (1982) Formation and distribution of mg, Fe, Mn-smectites in the first stages of the lateritic weathering of forsterite and tephroite. *Clay Minerals*, 17, 339–348.
- Nahon, D.B. and Colin, F. (1982) Chemical weathering of orthopyroxenes under lateritic conditions. *American Journal of Science*, 282, 1232–1243.
- Ohta, A. and Kawabe, I. (2001) REE(III) adsorption onto Mn dioxide (δ -MnO₂) and Fe oxyhydroxide: Ce(III) oxidation by δ -MnO₂. *Geochimica et Cosmochimica Acta*, 65, 695–703.
- Putzolu, F., Abad, I., Balassone, G., Boni, M., Cappelletti, P., Graziano, S.F., Maczurad, M., Mondillo, N., Najorka, J. and Santoro, L. (2020) Parent rock and climatic evolution control on the genesis of Ni-bearing clays in Ni-co laterites: new inferences from the Wingellina deposit (Western Australia). *Ore Geology Reviews*, 120, 24.
- Putzolu, F., Balassone, G., Boni, M., Maczurad, M., Mondillo, N., Najorka, J. and Pirajno, F. (2018) Mineralogical association and Ni-co deportment in the Wingellina oxide-type laterite deposit (Western Australia). *Ore Geology Reviews*, 97, 21–34.
- Putzolu, F., Boni, M., Mondillo, N., Maczurad, M. and Pirajno, F. (2019) Ni-co enrichment and high-tech metals geochemistry in the Wingellina Ni-co oxide-type laterite deposit (Western Australia). *Journal of Geochemical Exploration*, 196, 282–296.
- Qin, H.-B., Yang, S., Tanaka, M., Sanematsu, K., Arcilla, C. and Takahashi, Y. (2020) Chemical speciation of scandium and yttrium in laterites: new insights into the control of their partitioning behaviors. *Chemical Geology*, 552, 119771.
- Reith, F., Campbell, S.G., Ball, A.S., Pring, A. and Southam, G. (2014) Platinum in earth surface environments. *Earth-Science Reviews*, 131, 1–21.
- Rivera, J., Reich, M., Schoenberg, R., Gonzalez-Jimenez, J.M., Barra, F., Aiglsperger, T., Proenza, J.A. and Carretier, S. (2018) Platinum-group element and gold enrichment in soils monitored by chromium stable isotopes during weathering of ultramafic rocks. *Chemical Geology*, 499, 84–99.
- Roque-Rosell, J., Mosselmans, J.F.W., Proenza, J.A., Labrador, M., Gali, S., Atkinson, K.D. and Quinn, P.D. (2010) Sorption of Ni by "lithiophorite-asbolane" intermediates in Moa Bay lateritic deposits, eastern Cuba. *Chemical Geology*, 275, 9–18.
- Sassani, D.C. and Shock, E.L. (1998) Solubility and transport of platinum-group elements in supercritical fluids: summary and estimates of thermodynamic properties for ruthenium, rhodium, palladium, and platinum solids, aqueous ions, and complexes to 1000 degrees C and 5 kbar. *Geochimica et Cosmochimica Acta*, 62, 2643–2671.
- Schellmann, W. (1989) Composition and origin of lateritic nickel ore at Tagaung-Taung, Burma. *Mineralium Deposita*, 24, 161–168.

- Simandjuntak, T.O., Rusmana, E., Surono and Supandjono, J.B. (1991) *Peta Geologi Lembar Malili Sulawesi*. Bandung: Pusat Penelitian dan Pengembangan Geologi.
- Sufriadin, Idrus, A., Pramumijoyo, S., Warmada, I.W., Nur, I. and Imai, A. (2011) Mineralogical transformation and element distribution in two weathering profiles of the Soroako nickel laterite mining district, Sulawesi, Indonesia. *International Symposium on Earth Science and Technology*, 2011, 447–454.
- Suratman. (2000) Geology of laterite nickel deposit in Sorowako area, South Sulawesi Province. In *Proceedings of 29th Indonesian Association of Geologists, Bandung, Indonesia*, pp. 37–43.
- Tauler, E., Lewis, J.F., Villanova-de-Benavent, C., Aiglsperger, T., Proenza, J.A., Domenech, C., Gallardo, T., Longo, F. and Gali, S. (2017) Discovery of Ni-smectite-rich saprolite at Loma Ortega, Falcondo mining district (Dominican Republic): geochemistry and mineralogy of an unusual case of “hybrid hydrous mg silicate - clay silicate” type Ni-laterite. *Mineralium Deposita*, 52, 1011–1030.
- Teitler, Y., Cathelineau, M., Ulrich, M., Ambrosi, J.P., Munoz, M. and Sevin, B. (2019) Petrology and geochemistry of scandium in new Caledonian Ni-co laterites. *Journal of Geochemical Exploration*, 196, 131–155.
- Thorne, R.L., Roberts, S. and Herrington, R. (2012) Climate change and the formation of nickel laterite deposits. *Geology*, 40, 331–334.
- Traore, D., Beauvais, A., Auge, T., Parisot, J.C., Colin, F. and Cathelineau, M. (2008a) Chemical and physical transfers in an ultramafic rock weathering profile: part 2. Dissolution vs. accumulation of platinum group minerals. *American Mineralogist*, 93, 31–38.
- Traore, D., Beauvais, A., Chabaux, F., Peiffert, C., Parisot, J.C., Ambrosi, J.P. and Colin, F. (2008b) Chemical and physical transfers in an ultramafic rock weathering profile: part 1. Super-gene dissolution of Pt-bearing chromite. *American Mineralogist*, 93, 22–30.
- Trescases, J.J. (1975) L'évolution géochimique supergène des roches ultrabasiques en zone tropicale: formation des gisements nickélifères de Nouvelle-Calédonie. *Mémoires ORSTOM (Office de la Recherche Scientifique et Technique Outre-Mer)*, 78, 259.
- Ulrich, M., Cathelineau, M., Munoz, M., Boiron, M.C., Teitler, Y. and Karpoff, A.M. (2019) The relative distribution of critical (Sc, REE) and transition metals (Ni, Co, Cr, Mn, V) in some Ni-laterite deposits of New Caledonia. *Journal of Geochemical Exploration*, 197, 93–113.
- van Leeuwen, T. and Pieters, P.E. (2011) Mineral deposits of Sulawesi. *Sulawesi Mineral Resources 2011 Seminar MGEI-IGI, Manado, Indonesia*, pp. 1–109.
- Villanova-de-Benavent, C., Domenech, C., Tauler, E., Gali, S., Tassara, S. and Proenza, J.A. (2017) Fe-Ni-bearing serpentines from the saprolite horizon of Caribbean Ni-laterite deposits: new insights from thermodynamic calculations. *Mineralium Deposita*, 52, 979–992.
- Villanova-de-Benavent, C., Nieto, F., Viti, C., Proenza, J.A., Gali, S. and Roque-Rosell, J. (2016) Ni-phylosilicates (garnierites) from the Falcondo Ni-laterite deposit (Dominican Republic): mineralogy, nanotextures, and formation mechanisms by HRTEM and AEM. *American Mineralogist*, 101, 1460–1473.
- Villanova-de-Benavent, C., Proenza, J.A., Gali, S., Garcia-Casco, A., Tauler, E., Lewis, J.F. and Longo, F. (2014) Garnierites and garnierites: textures, mineralogy and geochemistry of garnierites in the Falcondo Ni-laterite deposit, Dominican Republic. *Ore Geology Reviews*, 58, 91–109.
- Wang, W.W., Pranolo, Y. and Cheng, C.Y. (2011) Metallurgical processes for scandium recovery from various resources: a review. *Hydrometallurgy*, 108, 100–108.

SUPPORTING INFORMATION

Additional supporting information may be found online in the Supporting Information section at the end of this article.

How to cite this article: Ito A, Otake T, Maulana A, Sanematsu K, Sufriadin, Sato T. Geochemical constraints on the mobilization of Ni and critical metals in laterite deposits, Sulawesi, Indonesia: A mass-balance approach. *Resource Geology*. 2021;1–28. <https://doi.org/10.1111/rge.12266>